

Role of Resolved and Parameterized Eddies in the Labrador Sea Balance of Heat and Buoyancy

OLEG A. SAENKO,* FRÉDÉRIC DUPONT,⁺ DUO YANG,* PAUL G. MYERS,[#]
IGOR YASHAYAEV,[@] AND GREGORY C. SMITH[&]

* Canadian Centre for Climate Modelling and Analysis, Environment Canada, Victoria, British Columbia, Canada

⁺ Canadian Meteorological Centre, Environment Canada, Dorval, Quebec, Canada

[#] Department of Earth and Atmospheric Sciences, University of Alberta, Edmonton, Alberta, Canada

[@] Bedford Institute of Oceanography, Fisheries and Oceans Canada, Dartmouth, Nova Scotia, Canada

[&] Meteorological Research Division, Environment Canada, Dorval, Quebec, Canada

(Manuscript received 6 March 2014, in final form 19 September 2014)

ABSTRACT

Deep convection in the Labrador Sea is an important component of the global ocean ventilation. The associated loss of heat to the atmosphere from the interior of the sea is thought to be mostly supplied by mesoscale eddies, generated either remotely or as a result of convection itself—processes that are not resolved by low-resolution ocean climate models. The authors first employ a high-resolution ($1/12^\circ$) ocean model forced with high-resolution (33 km, 3 h) atmospheric fields to further elaborate on the role of mesoscale eddies in maintaining the balance of heat and buoyancy in the Labrador Sea. In general agreement with previous studies, it is found that eddies remove heat along the coast and supply it to the interior. Some of the eddies that are generated because of the barotropic instability off the west coast of Greenland are recaptured by the boundary current. In the region of deep convection, the convergence of heat and buoyancy by eddies significantly increases with the deepening of the winter mixed layer. In addition, the vertical eddy flux plays an important part in the heat budget of the upper Labrador Sea, accounting for up to half of the heat loss to the atmosphere north of 60°N . A low-resolution (1°) model with parameterized eddies is then applied to show that it does capture, qualitatively, the general structure of eddy buoyancy advection along the Labrador Current. However, the 1° model is deficient in this regard in the most eddy active region off the west coast of Greenland, although some improvements can be made by forcing it with the high-resolution atmospheric fields.

1. Introduction

a. Background

Deep convection in the Labrador Sea is an important component of the global ocean ventilation and overturning circulation (McCartney 1992). It occurs in a limited area of the sea (e.g., Lavender et al. 2000; Pickart et al. 2002) and typically does not seem to reach below 1750-m depth (e.g., Lilly et al. 1999). During some years, however, the Labrador Sea convection can penetrate to more than 2-km depth (Lazier et al. 2001), injecting a weakly stratified water [the Labrador Sea Water (LSW)] into the deep western boundary current (DWBC) (McCartney 1992; Pickart et al. 1997, 2002; Palter et al. 2008). The

LSW has been found in many places of the middepth North Atlantic (Yashayaev et al. 2007) and beyond (Talley and McCartney 1982). It has also been associated with a maximum of chlorofluorocarbons in the North Atlantic (Smethie et al. 2000), suggesting a potentially important role of the LSW in taking up atmospheric gases and moving them to large depths. The strength of the Labrador Sea deep convection varies (e.g., Lazier et al. 2002; Yashayaev and Loder 2009) and on decadal time scales it apparently does so out of phase with convection in other regions of the North Atlantic Ocean (Dickson et al. 1996). There is also some observational evidence suggesting that the process of LSW formation does not appear to be merely a passive response to atmospheric forcing, such as strong westerly winds and surface heat loss. Rather, the associated extraction of heat from the deeper ocean, or the lack thereof, can have a strong impact on fluctuations of the surface climate. Such fluctuations, “imprinted” in the

Corresponding author address: Oleg A. Saenko, Canadian Centre for Climate Modelling and Analysis, Environment Canada, 3800 Finnerty Rd., Victoria BC V8P 5C2, Canada.
E-mail: oleg.saenko@ec.gc.ca

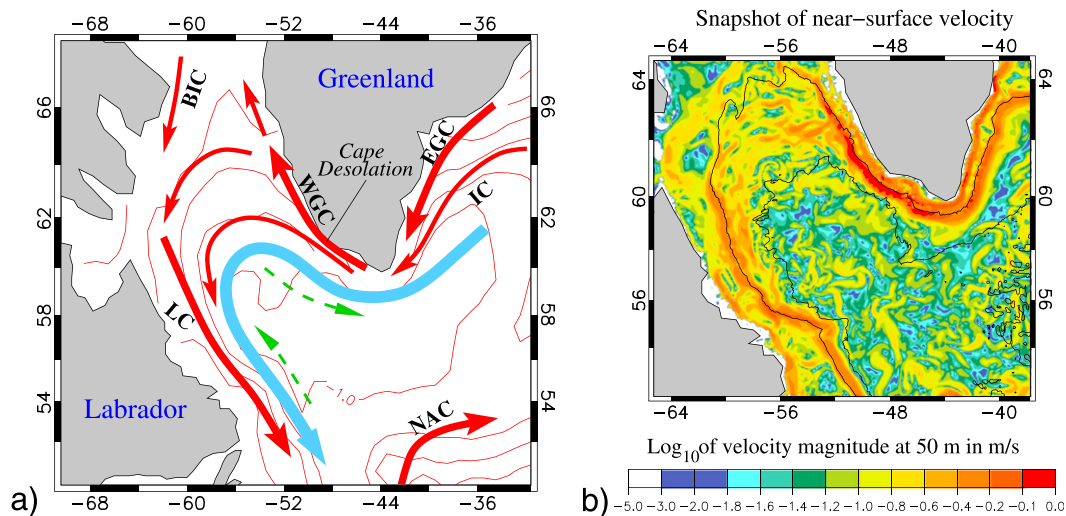


FIG. 1. (a) A schematic view of the Labrador Sea major currents, based in part on the circulation maps presented by Lavender et al. (2000, their Fig. 2) and Cuny et al. (2002, their Fig. 4): East Greenland Current (EGC), West Greenland Current (WGC), Irminger Current (IC), Baffin Island Current (BIC), Labrador Current (LC), and North Atlantic Current (NAC). Dashed arrows indicate middepth recirculations reported by Lavender et al. (2000), whereas the blue arrow is to illustrate the flow of DWBC. Shown with red contours on the background is the mean (1992–2002) sea surface height (m; contour interval = -0.1 m) estimated based on satellite altimetry (Maximenko and Niiler 1999). (b) A “snapshot” (2-day average; 21–23 Mar 2005) of near-surface speed simulated by the $1/12^\circ$ model. Also displayed (thin lines) are the 1- and 3-km isobaths as resolved by the model bathymetry.

upper Labrador Sea can penetrate deep into the subtropical Atlantic (Curry et al. 1998).

Despite its importance, much remains unknown about the Labrador Sea ventilation and the associated heat budget. This is in part because of the difficulties involved in obtaining in situ measurements in its harsh environment [described, e.g., in section 3 of Pickart et al. (2002)]. Some of the main known features of Labrador Sea large-scale circulation are shown in Fig. 1a. It is commonly understood that the loss of heat to the atmosphere is ultimately resupplied by the boundary currents, with mesoscale eddies carrying the heat into the sea interior (e.g., Lilly et al. 2003; Katsman et al. 2004; Straneo 2006; Hátún et al. 2007; Chanut et al. 2008; Spall 2004). However, how the balance of heat is maintained at subbasin scales, and the role of different eddy types, is less known. Observations (e.g., Lilly et al. 2003) and high-resolution numerical simulations (e.g., Chanut et al. 2008) suggest that there are at least three types of eddies in the Labrador Sea, which all could have a sizable contribution to balancing the loss of buoyancy at the surface. First, there are the Irminger rings (IR)—energetic warm-core eddies, originating from the Irminger Current in the region of enhanced eddy kinetic energy (EKE) off the west coast of Greenland. Their trajectories, either observed (Hátún et al. 2007) or derived from maps of EKE (Lilly et al. 2003), can be used to understand why the region of deep convection is small (presenting a major

challenge for low-resolution ocean models). Second, there are boundary current eddies (BCEs). These represent less energetic instabilities, generated all along the boundary current system, including along the coast of Labrador. The associated lateral eddy fluxes, studied by Spall (2004) and more recently by McGeehan and Maslowski (2011), also can represent an effective mechanism for offsetting the loss of buoyancy in the Labrador Sea interior. Finally, the eddies associated with baroclinic instability of the convective patch itself [convective eddies (CEs)] can rapidly disperse a weakly stratified water column (Visbeck et al. 1996; Jones and Marshall 1997), thereby playing an important role in the rapid (several months) postconvective restratification of the Labrador Sea.

However, assessing the role of different eddy types in restratifying the Labrador Sea is a very complex subject. One reason for this is that each of these eddy types may strongly influence the Labrador Sea stratification and each other. Gelderloos et al. (2011) derived restratification time scales for different eddy types for the case of cone-shaped convection area, assuming a constant ambient stratification. However, the observed stratification in the Labrador Sea is strongly surface intensified [as also pointed out by Jones and Marshall (1997)]. As such, while we also attempt to estimate the time scales of Labrador Sea restratification due to different eddy types, using the scaling relations of

Gelderloos et al. (2011), such estimates should be taken with caution.

b. Objectives

One objective of the present study is to obtain further insight about the role of eddies in maintaining a time-mean budget of heat in the Labrador Sea. The focus is on the region of deep convection, as well as on the broader area of the sea. Some aspects of this subject have been addressed before in several studies using observations, theories, and models (e.g., Jones and Marshall 1997; Houghton and Visbeck 2002; Katsman et al. 2004; Spall 2004; Straneo 2006; Hátún et al. 2007; Chanut et al. 2008). Yet, our understanding of the relative roles played by eddies and mean currents in the Labrador Sea balance of heat is incomplete and will be addressed here using a $1/12^\circ$ model forced with high-resolution (33 km, 3 h) atmospheric fields (see next section). Of particular relevance to this subject are the studies by Chanut et al. (2008) and more recently by Kawasaki and Hasumi (2014), who, among other insightful results, present integrated budgets of heat and buoyancy based on high-resolution models forced with monthly climatology. In particular, Chanut et al. find that, on the basin scale, the heat required to balance its loss to the atmosphere is supplied by the large-scale circulation; it is then redistributed to the Labrador Sea interior almost exclusively by eddies.

Here, we further elaborate on this subject in several ways. First, we take a closer look at the convergence of heat by eddies in the Labrador Sea interior, focusing on the region of deep mixing in winter. In particular, there are reasons to expect that the heat convergence by eddies may increase with the deepening of convective mixing and with stronger heat loss at the surface (e.g., Jones and Marshall 1997). However, observations indicate that the areas of strongest surface heat loss in the Labrador Sea are not collocated with the deepest mixed layers (e.g., Lavender et al. 2000; Cuny et al. 2002). In addition, the transport of heat by the mean currents may also be important, particularly in the regions close to the boundary current system (Chanut et al. 2008). Indeed, it has been estimated, using Lagrangian floats, that the heat fluxes associated with the mean circulation in the Labrador Sea region of deep convection could amount to 30% of the eddy heat fluxes (Palter et al. 2008).

Second, we consider budgets of heat and buoyancy. While observations seem to indicate that the structure of eddies in the Labrador Sea is dominated by temperature (Lilly and Rhines 2002; Pickart et al. 2002), the input of freshwater from the eddies, required to account for the spring restratification of convective areas, cannot be ignored (Hátún et al. 2007). Modeling studies do suggest

that freshwater anomalies from the Labrador shelf (Myers 2005; McGeehan and Maslowski 2011) and from the region off the west coast of Greenland (Kawasaki and Hasumi 2014) can have a strong impact on the deep convection, particularly in sufficiently high-resolution models. It has also been observed that the waters entering and leaving the Labrador Sea on the same isopycnal level may have significantly different thermohaline properties (Palter et al. 2008). This suggests that the budgets of heat and buoyancy, while expected to be similar in general, may differ in details.

Third, we shall separate the eddy buoyancy flux into lateral and vertical components. While the role of lateral eddy fluxes in the Labrador Sea has been widely appreciated, this cannot be said about the role of vertical eddy fluxes. Physically, the latter implies a transfer of eddy potential energy (EPE) to EKE. We find the upward eddy buoyancy flux to be particularly strong north of the deep convection region, likely because of the propagation of IRs and conversion of their EPE to EKE as they move southwestward. The associated supply of heat from the deeper ocean to the surface layer represents a significant fraction of heat loss to the atmosphere in the region.

Our second objective is to evaluate the extent to which low-resolution models can represent buoyancy fluxes in the Labrador Sea by parameterized eddies. It is still not uncommon to employ models with resolution of $\sim 1^\circ$ to study deep-water formation/convection in the Labrador Sea, its variability and changes in response to changes in climate. The validity of conclusions made based on such models remains unclear, given the importance of mesoscale eddies in the Labrador Sea. Typically, and this is also the case here, low-resolution ocean climate models employ the Gent and McWilliams (1990, hereafter GM90) parameterization to represent some of the effects arising due to mesoscale eddies. In particular, this parameterization mimics a local removal of potential energy by eddies from mean baroclinic currents. However, it has been argued that nonlocal eddy effects can also be very important in the Labrador Sea (e.g., Hátún et al. 2007; Chanut et al. 2008). Moreover, some studies conclude that it is barotropic, rather than baroclinic, instability that dominates the generation of the most energetic eddies off the west coast of Greenland (Eden and Böning 2002). In addition, deep convection in the Labrador Sea is a highly localized process (Clarke and Gascard 1983; Lavender et al. 2000; Pickart et al. 2002; see also section 3), with the radius of convective patch being of the order of 100 km. Therefore, the applicability of low-resolution models for studying the Labrador Sea dynamics, including its changes under global warming scenarios, remains unclear. Here, we only

touch on one aspect of this important subject; namely, on the sensitivity of the eddy-induced buoyancy transport in the Labrador Sea to atmospheric forcing.

The paper is organized as follows: [Section 2](#) describes the employed numerical models and atmospheric forcing data. Some features of the simulated and observed Labrador Sea circulation are discussed in [section 3](#). Budgets of heat and buoyancy in our high-resolution model are analyzed in [section 4](#). In [section 5](#), we illustrate the sensitivity of the Labrador Sea circulation and eddy buoyancy convergence simulated by a low-resolution model to atmospheric forcing. Discussion and conclusions are presented in [section 6](#).

2. Models, forcing data, and observations

a. Numerical models

We employ two configurations of the Nucleus for European Modeling of the Ocean model (NEMO; [Madec 2008](#); [Madec et al. 2012](#)). One is a regional high-resolution model based on the NEMO ORCA12 configuration developed within the Mercator-Ocean and DRAKKAR collaboration ([Barnier et al. 2007](#)). It has a horizontal resolution of $1/12^\circ$ (on Mercator grid) and 50 vertical levels. The model bathymetry is based on 2-Min Gridded Global Relief Data (ETOPO2) ([Le Galloudec et al. 2008](#)); the minimum and maximum depths are set at 20 and 5750 m. We shall refer to this model as eddy resolving, although given the size of the eddies observed in the Labrador Sea, with radii ranging from 5 to 30 km ([Lilly et al. 2003](#)), and given the local Rossby radius, the $1/12^\circ$ resolution is still perhaps only eddy permitting. The lateral mixing of momentum is represented by biharmonic viscosity with a coefficient of $-1 \times 10^{10} \text{ m}^4 \text{ s}^{-1}$. For unresolved lateral mixing of tracers, the model employs an isopycnal Laplacian framework with a diffusivity of $50 \text{ m}^2 \text{ s}^{-1}$. The enhanced mixing in the upper ocean is parameterized according to the turbulent closure model of [Gaspar et al. \(1990\)](#); see also [Blanke and Delecluse 1993](#)). The background values for vertical viscosity and diffusivity are set, respectively, to 10^{-4} and $10^{-5} \text{ m}^2 \text{ s}^{-1}$.

The $1/12^\circ$ model simulation was performed in the framework of the Canadian Operational Network of Coupled Environmental Prediction Systems (CONCEPTS) on a regional domain (CREG12). The CREG12 domain covers the North Atlantic Ocean north of 27°N , as well as the whole Arctic Ocean ([F. Dupont et al. 2014](#), unpublished manuscript). As such, the narrow Canadian Arctic Archipelago passages—one of the two pathways through which a low salinity Arctic Ocean water enters the Labrador Sea—are represented. This is essential, for

example, for a shelf-to-interior freshwater transport along the coast of Labrador (e.g., [McGeehan and Maslowski 2011](#)). The CREG12 simulation was initialized on 1 January 2003 from a global Mercator-Ocean ORCA12 simulation (e.g., [Le Galloudec et al. 2008](#)) and forced with high-frequency atmospheric forcing (see next subsection). The model output used here are 2-day averages, covering a 5-yr period, 2003–07. This period is characterized by a progressive penetration of relatively warm waters to deeper layers in the Labrador Sea interior (see next section).

The second NEMO configuration that we employ has a global domain with a nominal resolution of 1° on the ORCA1 grid (refined to $1/3^\circ$ meridionally near the equator) and with 46 vertical levels. The lateral mixing of momentum is represented by a Laplacian operator with a nominal value of viscosity coefficient, which varies with local resolution, set to $1 \times 10^4 \text{ m}^2 \text{ s}^{-1}$. While such relatively coarse resolution is often employed in ocean models for climate and paleoclimate simulations, it does not allow for the processes associated with ocean mesoscale eddies to be explicitly resolved. Instead, they are parameterized. Most commonly, including here, this is done through a parameterized eddy contribution to advection and diffusion of tracers. Essentially, the tracers are mixed along isopycnal (isoneutral) surfaces (e.g., [Redi 1982](#)) using the accordingly rotated Laplacian operator. The corresponding coefficient is set to $10^3 \text{ m}^2 \text{ s}^{-1}$ near the equator and decreases with latitude to values of $5 \times 10^2 \text{ m}^2 \text{ s}^{-1}$ around 60°N/S . In addition, the removal of energy from the mean baroclinic currents is represented by the GM90 scheme. The associated eddy-induced transport velocities are proportional to the eddy transfer coefficient, or layer thickness diffusivity K ([Gent et al. 1995](#); see also the [appendix](#)). A spatially varying formulation is employed, such that $K \propto L^2 T^{-1}$, where L and T are, respectively, the eddy mixing length and time scales. In the model, L is set by the local Rossby radius (outside of the equatorial region), whereas T is given by the [Eady \(1949\)](#) time scale for the growth rate of unstable baroclinic instabilities, similar to [Visbeck et al. \(1997\)](#). As in the $1/12^\circ$ model, the enhanced mixing in the upper ocean is parameterized based on the model of [Gaspar et al. \(1990\)](#), with the same background values for vertical viscosity and diffusivity. Both the $1/12^\circ$ and 1° models use a linear free-surface formulation (see, e.g., [Madec et al. 2012](#), and references therein).

In addition, both model configurations have sea ice components and use bulk formulations to obtain fluxes of heat, water, and momentum. To calculate these fluxes, we use several atmospheric products. These are described in the next subsection.

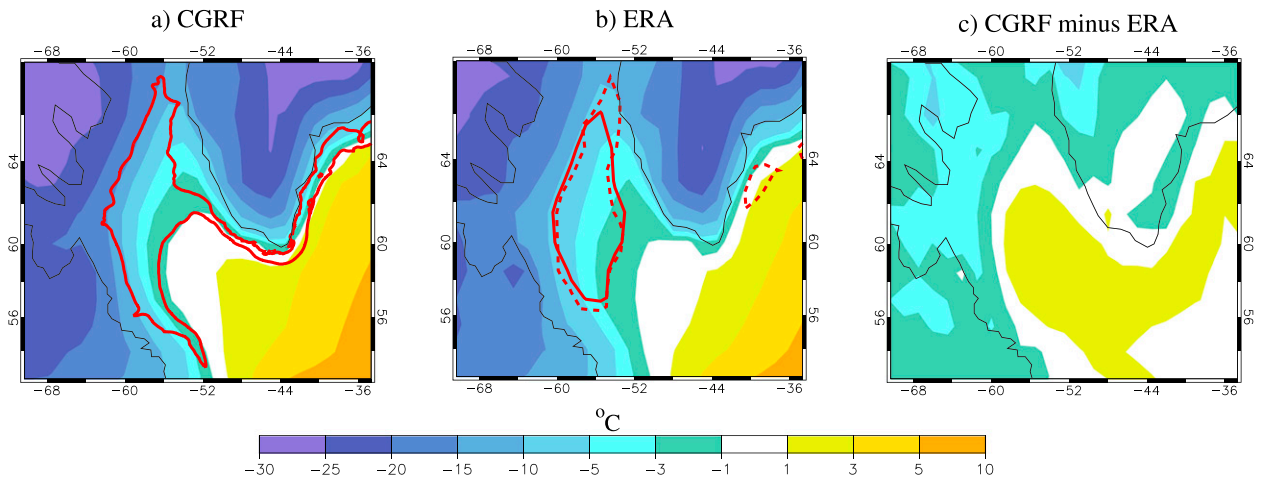


FIG. 2. Mean winter (January–March, 2003–07) 2-m air temperature, corresponding to the (a) CGRF and (b) ERA-Interim product and (c) the air temperature difference (CGRF minus ERA-Interim). Solid red contours indicate the regions inside of which the corresponding mean winter heat loss exceeds 250 W m^{-2} in (a) (in the $1/12^\circ$ model forced with the CGRF atmospheric data; see text for details) and 150 W m^{-2} in (b) (based on ERA-Interim heat fluxes). In addition, the dashed contour in (b) shows the regions inside of which the mean (2003–07) winter heat loss exceeds 200 W m^{-2} in the WHOI heat flux product (<http://oafux.whoi.edu/>). Different values are used for the heat flux contours in order to indicate the regions of enhanced heat loss that cover roughly the same area in the three data products.

b. Forcing data

The $1/12^\circ$ CREG12 model is forced with atmospheric fields that have resolution of 33 km in space and, as used here, 3 h in time (Smith et al. 2013). They are derived from the Canadian Meteorological Centre (CMC)'s global deterministic prediction system (GDPS). Smith et al. (2013) compared global near-surface temperature, humidity, and winds from CMC GDPS reforecasts (CGRF product hereinafter) with several observation-based atmospheric products, including with the Interim European Centre for Medium-Range Weather Forecasts (ECMWF) Re-Analysis (ERA-Interim) (Dee et al. 2011). They found, in particular, that the higher resolution of the CGRF product provides a more detailed representation of atmospheric structures and topographic steering, compared to ERA-Interim product, resulting in finer-scale coastal features and wind stress curl. Focusing on the Labrador Sea, Fig. 2 compares the 2-m mean (2003–07) air temperature in winter from the CGRF and ERA-Interim. While the temperature structure is similar between the two atmospheric products, the CGRF has stronger temperature gradients over the western part of the Labrador Sea, with colder temperatures in the west and warmer in the Labrador Sea interior (Fig. 2c).

Also displayed in Fig. 2 are the regions where the mean 2003–07 winter surface heat loss is largest: in the $1/12^\circ$ model forced with the CGRF data (Fig. 2a) and in two observation-based products, the ERA-Interim (Dee et al. 2011) and Woods Hole Oceanographic Institution (WHOI) (Yu et al. 2004) (Fig. 2b). In general, the rate of

winter heat loss to the atmosphere is lower in the observation-based products compared to that in the model. This could be one of the reasons for weaker than observed stratification simulated by the model, and for deeper than observed penetration of convective mixing discussed in section 3. However, the difference between the observation-based estimates is also large, being comparable to the model–observation difference. This reflects the uncertainty in observation-based estimates, which is particularly large during winter months (cf. Fig. 13a). In addition, we note that the region of greatest heat loss to the atmosphere in the two observation-based products (Fig. 2b) only partly overlaps with the region of deepest winter mixing during the 2003–07 time interval reported by Våge et al. (2009). This is consistent with Lavender et al. (2000), who observed the greatest winter heat loss ($345 \pm 95 \text{ W m}^{-2}$) in the northern third of the Labrador Sea basin, whereas the central portion of the basin with the deepest mixed layers had, in their observations, an average winter heat loss of only $49 \pm 46 \text{ W m}^{-2}$. The subject certainly requires more research (Moore et al. 2014).

In addition, station-based observations suggest that the Labrador Sea surface buoyancy flux has a significant high-frequency variability (Sathiyamoorthy and Moore 2002), attributable to the passage of synoptic weather systems. As such, accounting for this atmospheric variability could be essential for the Labrador Sea dynamics and heat budget. Hereinafter, the $1/12^\circ$ CREG12 model simulation forced with the 33 km, 3 h CGRF atmospheric data is referred to as CREG12-CGRF.

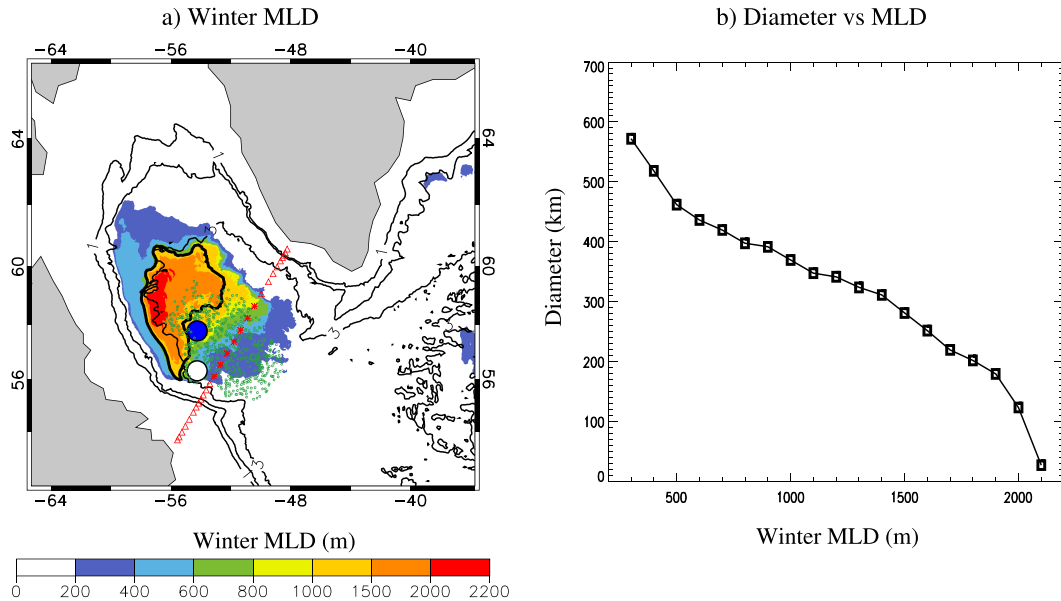


FIG. 3. (a) Mean winter (January–March, 2003–07) MLD defined as the depth where potential density σ_θ exceeds its surface value by 0.005 kg m^{-3} (Chanut et al. 2008; see also Fig. 11 in Pickart et al. 2002). Thick solid contour represents mean winter $\sigma_\theta = 27.79$ at about 100-m depth. The large white circle indicates the region where Pickart et al. (2002) observed mixed layers as deep as 1400 m during winter of 1997 (their Fig. 12d), whereas the blue circle approximately indicates the region of deepest mixed layers observed in winter (February–April) from 2000 to 2007 (Våge et al. 2009, their Fig. 2) that, however, did not exceed 900 m on average. The green symbols indicate the locations of Argo data used in the lower panel of Fig. 4, whereas the red symbols show the standard AR7W station positions (the stations used in the lower panel of Fig. 4 are shown with asterisks). Also displayed (thin lines) are the 1-, 2-, and 3-km isobaths. (b) Effective diameter of the model convective patch [defined as $d_{\text{eff}} = 2(A/\pi)^{1/2}$, with A being the area], plotted as function of mean winter MLD.

We also discuss simulations based on the 1° (NEMO ORCA1) model. One set of such simulations is forced with the CGRF atmospheric forcing (hereafter ORCA1-CGRF), where we test the sensitivity of the eddy-induced advection of buoyancy to the frequency of the forcing. In addition, the 1° model is forced with two climatological products. One of them was compiled based on the atmospheric fields described by Large and Yeager (2009). This product has been widely employed, including forcing ocean–ice models in the Coordinated Ocean Research Experiments (CORE product hereinafter; Griffies et al. 2009; Danabasoglu et al. 2014). The CORE product is based on National Centers for Environmental Prediction (NCEP) reanalysis and consist of 1) 6-h near-surface winds, air temperature, and humidity; 2) daily shortwave and incoming longwave radiation; and 3) monthly precipitation. We shall refer to the corresponding NEMO ORCA1 simulation as to ORCA1-CORE.

The second climatology that we employ to force the NEMO ORCA1 model was derived by averaging daily atmospheric data from a climate model simulation. The latter is based on the fully coupled Second Generation Canadian Earth System Model (CanESM2) developed at the Canadian Centre for Climate Modeling and

Analysis (see Yang and Saenko 2012, and references therein). As such, the corresponding atmospheric fields are not constrained by any observations. We shall refer to the NEMO ORCA1 model forced with the CanESM2 data as to ORCA1-CanESM2.

c. Observations

Since 1990, the Ocean and Ecosystem Sciences Division at the Bedford Institute of Oceanography has carried out annual occupations of a hydrographic section across the Labrador Sea (Yashayaev 2007). The section was designated the Atlantic Repeat Hydrography Line 7 West (AR7W) in the World Ocean Circulation Experiment (WOCE). This line is the major component of the Canadian Department of Fisheries and Oceans (DFO) Atlantic Zone Off-Shelf Monitoring Program (AZOMP) and the main Canadian contribution to the international Global Climate Observing System (GCOS) and to the (international) Climate Variability and Predictability (CLIVAR) component of the World Climate Research Programme (WCRP). The section spans approximately 880 km from the 130-m contour on the inshore Labrador shelf to the 125-m contour on the West Greenland shelf (Fig. 3a).

After 2002 the annual hydrographic observations in the Labrador Sea are supplemented with year-round vertical profiles (throughout the top 2000-m layer) of temperature and salinity from a network of Argo floats drifting at fixed depths. DFO and Environment Canada (EC) are the two major Canadian supporters of the international Argo program ensuring continuous monitoring of oceanographic conditions in the Labrador Sea on seasonal to interannual time scales.

The observations from research ships were combined with the Argo floats data, which have a much better spatial coverage (Fig. 3a), to construct the time–depth distribution and time series of observed potential temperature (and salinity) in the central Labrador Sea (Yashayaev and Loder 2009). These are analyzed and used for model validation in the next section.

3. Circulation, mixed layer, and EKE

Surface drifters indicate three distinct speed regimes in the Labrador Sea (Cuny et al. 2002): fast boundary currents, a slower crossover from Greenland to Labrador, and a slow, eddy-dominated flow in the basin interior. This observational picture is reflected in the near-surface velocity simulated by our $1/12^\circ$ model (Fig. 1b). The mean currents, which dominate Fig. 1b along the boundaries, closely follow the bathymetry, as observed (e.g., Cuny et al. 2002; Lavender et al. 2000). In general, a weakly forced flow with a large barotropic component is expected to follow f/H contours, with f and H being, respectively, the Coriolis parameter and ocean depth.

One of the major challenges is to simulate the location and vertical extent of winter mixed layer depth (MLD), particularly when it comes to a specific time period. While observations remain sparse, it appears that models tend to overestimate the observed patterns of MLD (Chanut et al. 2008), and our model is not an exception in this regard. In particular, the 2003–07 mean winter MLD, estimated based on Argo float data, does not exceed 900 m (Våge et al. 2009). Furthermore, it is located in the Labrador Sea interior. In contrast, the model simulates the deepest winter MLD mostly along the 3-km isobath in the western part of the sea (Fig. 3a). However, while the region around the 3-km isobath may seem an unlikely location for LSW formation, as it receives a constant advective inflow of relatively warm and stratified Irminger Seawater, nonetheless a hydrographic cruise in February–March 1997 captured the formation of LSW on the slope in the region of the DWBC (Pickart et al. 2002; Palter et al. 2008; Lavender et al. 2000). The location of deep mixing may have important implications for eddy heat fluxes, particularly from the boundary into the interior (Spall 2004; Straneo 2006). As such, our

results may be more applicable to time periods characterized by deep convection in the Labrador Sea, enhanced along the slope region.

The effective diameter of the region with relatively large winter MLDs decreases roughly linearly with MLD for MLDs between 500 and 1700 m (Fig. 3b) but then drops sharply, being only about 100 km where the MLD is deeper than 2000 m. This illustrates that the region subject to the deepest convection can be very small and difficult to detect. For example, the area where MLD is deeper than 2000 m is about 15 times smaller than the area where MLD is deeper than 1000 m. In hydrographic observations (e.g., Lavender et al. 2000; Pickart et al. 2002), the smallness of the deep convection region could result from the data coverage being typically quite scarce. Argo floats, on the other hand, provide a means to sample throughout the convective season. However, as pointed out by Våge et al. (2009), they do so at a resolution that is also quite limited.

To validate the model, we combined hydrographic and Argo floats data (Yashayaev and Loder 2009; see also section 2c). The simulated and observed evolutions of mean potential temperature profiles in the central Labrador Sea are compared in Fig. 4. It should be noted that for a proper model–observation comparison, it is sometimes more instructive to focus on the specific phenomenon (e.g., convective mixing), rather than impose the same vertical and/or regional restrictions on model data and observations. This is the approach that we adopt in the model–observation comparison presented Figs. 4 and 5. In general, the model reproduces the observed seasonal cycle and gradual warming of the Labrador Sea from 2003 to 2008 (Fig. 4; see also Fig. 5, left panel). It also captures some details. For example, the observations suggest that the deep-reaching cooling episodes lasted somewhat longer during the winters of 2003 and 2005 than during the other three winters; this is captured by the model to some degree. However, the agreement with observations is less favorable in the deeper layers (Fig. 5, right panel). According to the model, the convective signal does penetrate at least to the 1000–1500-m layer, whereas it is much weaker, or absent altogether, in the observations.

The observations also reveal that during the 2003–07 period the salinity in the Labrador Sea interior was increasing (not shown). The rate of salinity increase was larger during the first 2 yr (2003 and 2004) than during the last 3 yr (2005–07), with the mean rate of about $5 \times 10^{-3} \text{ g kg}^{-1} \text{ yr}^{-1}$ in the upper 1500-m-thick layer. The model salinity trend has the same sign, but with the rate of salinity increase being comparable to the observed rate only during the first 2 yr; otherwise, it is 2 times larger. This reflects a well-known problem of model

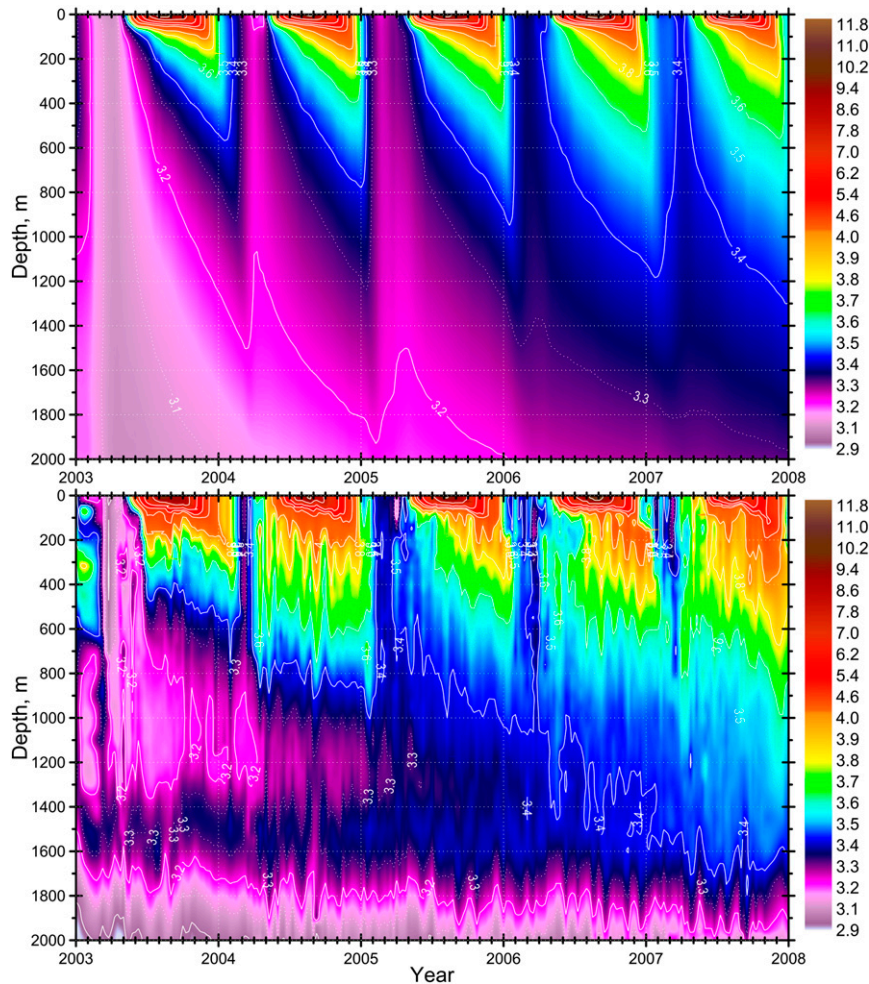


FIG. 4. Evolution of potential temperature profiles ($^{\circ}\text{C}$) in the Labrador Sea interior: (upper) in the model and (lower) in the observations of Yashayaev and Loder (2009). In the model, the averaging is applied over the region where the mean winter MLD exceeds 1000 m (see Fig. 3a); the spatial coverage of the data used in the lower panel is also shown in Fig. 3a.

salinity drift (e.g., Treguier et al. 2005). Unlike in the case of ocean–atmosphere thermal coupling, the ocean–atmosphere feedback with respect to hydrological cycle is weak (e.g., Weaver and Hughes 1992). Furthermore, the salinity drift can be further amplified in ocean models forced with freshwater flux consisting of prescribed precipitation and internally computed (from the latent heat loss) evaporation, such as in our model.

In addition, the model simulates the largest values of MLD somewhat too far north. This could be attributed to the position of the EKE maximum off the west coast of Greenland, associated with IRs. Indeed, given the importance of IRs (e.g., Gelderloos et al. 2011), it seems reasonable to expect that their more northward generation would result in a more northward location of deep mixing in the Labrador Sea. In the model, the pattern of enhanced EKE associated with IRs is too far north,

compared to observational estimates¹ (Fig. 6a). Some other models are more successful in this regard. For example, in the model of Luo et al. (2011) the EKE maximum is $\sim 0.5^{\circ}$ farther south. However, the general pattern of EKE in Luo et al. (2011) is similar to our model.

The simulated Labrador Sea EKE has a pronounced seasonal cycle (Fig. 6b). The model also suggests that EKE decays sharply with depth, being several times larger at the surface than at 100-m depth. This should be kept in mind when comparing observationally based

¹ The presented observational estimate of EKE was obtained based on gridded AVISO satellite data. As such, while it may provide the right general pattern of enhanced EKE off the west coast of Greenland, the EKE magnitude is most likely underestimated.

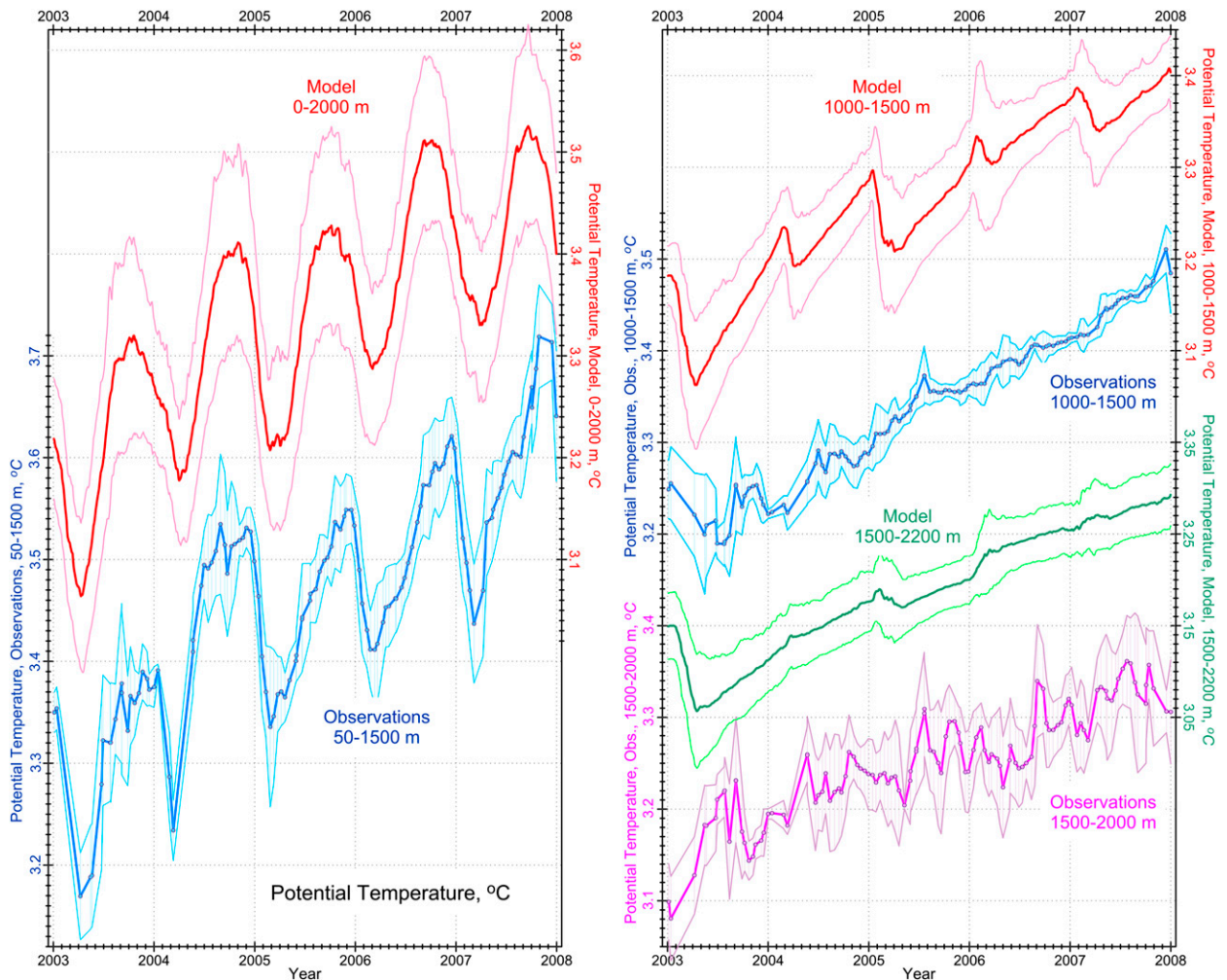


FIG. 5. Evolution of simulated and observed potential temperature shown in Fig. 4, except averaged vertically (left) over the whole water column subject to winter mixing and (right) over the two layers in the deep portion of the water column. Thin curves indicate ranges of spatial variability, given by ± 1 standard deviation. The depth ranges are not always the same to better cover similar density layers in the model data and observations.

EKE fields with EKE simulated by models at different depths. In the CREG12-CGRF, the enhanced level of EKE near the surface is also likely reinforced by the high-frequency atmospheric forcing.

4. Budgets of heat and buoyancy in the high-resolution model

A change of tracer C over a time period Δt can be written as a sum due to the advection by mean flows \mathcal{M} , eddy fluxes \mathcal{E} , and parameterized processes D :

$$\frac{\Delta C}{\Delta t} = \mathcal{M} + \mathcal{E} + D, \quad (1)$$

where

$$\mathcal{M} = -\bar{\mathbf{u}} \cdot \nabla \bar{C} - \bar{w} \partial_z \bar{C}, \quad \text{and} \quad (2)$$

$$\mathcal{E} = -\nabla \cdot (\overline{\mathbf{u}'C'}) - \partial_z (\overline{w'C'}), \quad (3)$$

with the overbar and prime representing, respectively, averaging over the time period Δt and deviation from the average (unless stated otherwise, $\Delta t = 5$ yr); ∇ is the 2D(x, y) gradient operator; and $[\mathbf{u}(u, v), w]$ is the velocity field. In what follows, C represents either the heat content (i.e., $C = \rho_0 c_p \theta$, where ρ_0 , c_p , and θ are, respectively, the reference density, specific heat, and potential temperature of water) or buoyancy (i.e., $C = -g\sigma/\rho_0$, where g and σ are, respectively, gravitational acceleration and potential density). The subgrid-scale term D is not calculated explicitly, but rather as the residual of the other

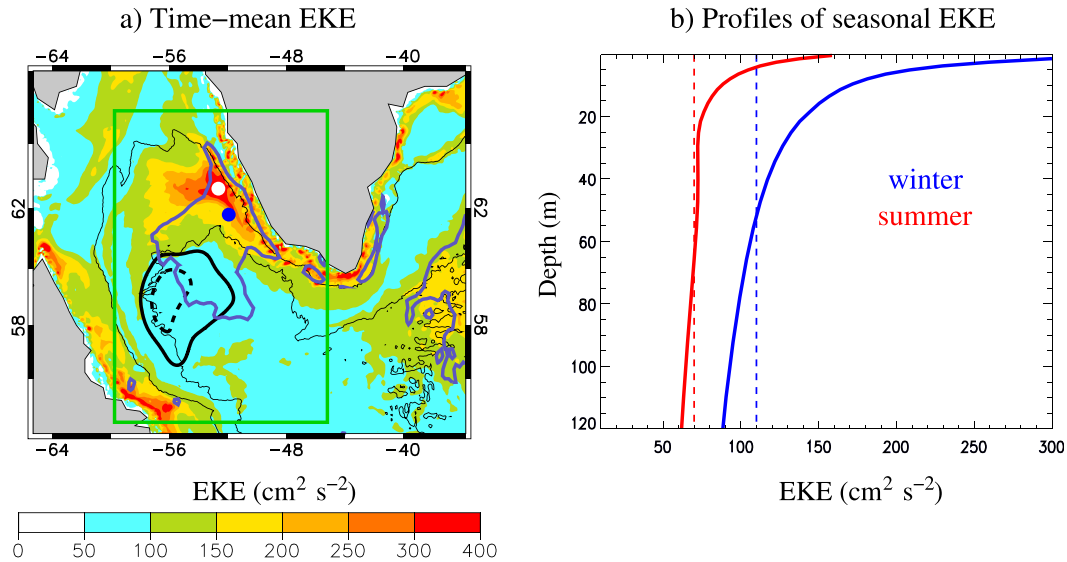


FIG. 6. (a) Time-mean EKE ($\text{cm}^2 \text{s}^{-2}$, color) simulated by the model at the surface during the period of interest. Thick black contours represent the regions inside of which the simulated depth of winter (January–March, 2003–07) MLD exceeds (solid) 1000 and (dashed) 1700 m (a smoothed version of MLD from Fig. 3a). The blue contour shows the region of enhanced (more than $50 \text{ cm}^2 \text{s}^{-2}$) near-surface EKE estimated based on the 2003–07 gridded Archiving, Validation, and Interpretation of Satellite Oceanographic data (AVISO) near-surface geostrophic velocity (see the acknowledgments). The blue and white circles show approximate locations of EKE maximum in, respectively, the AVISO data and model. Also displayed are (thin lines) the 1- and 3-km isobaths, as resolved by the model bathymetry. (b) Profiles of mean summer (July–September, 2003–07) and winter (January–March, 2003–07) EKE in the upper ocean averaged between 55° and 65°N and 60° and 45°W [which is the subregion indicated in (a) with the green box]. Also displayed (dashed vertical lines) are the amplitude of mean seasonal EKE variations estimated by White and Heywood (1995) for the same region using altimetric data (taken from the annual harmonic in their Fig. 7g).

three terms in Eq. (1). It combines convective mixing, turbulent diffusion, and surface forcing; in the case of buoyancy, it also includes some other effects, such as, for example, those arising because of the nonlinearities of the equation of state (e.g., Gnanadesikan et al. 2005).

a. Spatial structure

Figure 7 displays surface heat flux and vertically integrated advective terms of the heat budget. Consistent with Chanut et al. (2008, their Fig. 17) and with Kawasaki and Hasumi (2014, their Fig. 8), the total heat convergence due to the mean circulation and eddies [$\int (\mathcal{M} + \mathcal{E}) dz$] closely balances the loss of heat at the surface (Figs. 7a,b). This means that the tendency term, averaged over the period of interest, is relatively small. This is despite the fact that the CREG12-CGRF model is forced by an interannual atmospheric forcing, so that temperature does evolve (Figs. 4, 5). The largest heat loss at the surface is found away from the region of large MLDs, in the northwestern part of the basin (Fig. 7a; see also Fig. 2a). As already noted, the observations analyzed by Lavender et al. (2000) also suggest that the greatest surface heat loss in the Labrador Sea does not occur in the region of the

deepest mixed layers. (For the mixing to penetrate to large depths, factors other than surface heat flux can play an important role, including the background stratification, local circulation, wind stress curl, etc.) In the model of Chanut et al. (2008), which was forced with climatological atmospheric forcing, the largest time-mean rate of surface cooling reaches comparable values locally, but is simulated closer to the region of deep convection.

Decomposing the net advective heat flux into mean and eddy components shows a more complex structure (Figs. 7c,d), broadly consistent with Chanut et al. (2008). The most extreme values of the advective heat convergence, because of both the mean flows and eddies, are simulated off the west coast of Greenland; that is, in the region of highest EKE level (Fig. 6a). Locally, the mean and eddy fluxes reach $\pm 500 \text{ W m}^{-2}$ (Figs. 7c,d), generally tending to cancel each other. However, the advective input of heat by the mean boundary currents is not fully compensated by the eddy heat divergence. Instead, the $\int (\mathcal{M} + \mathcal{E}) dz$ residual is mostly balanced by the surface heat loss.

We next consider the corresponding budget of buoyancy (Fig. 8). In most of the Labrador Sea, the mean

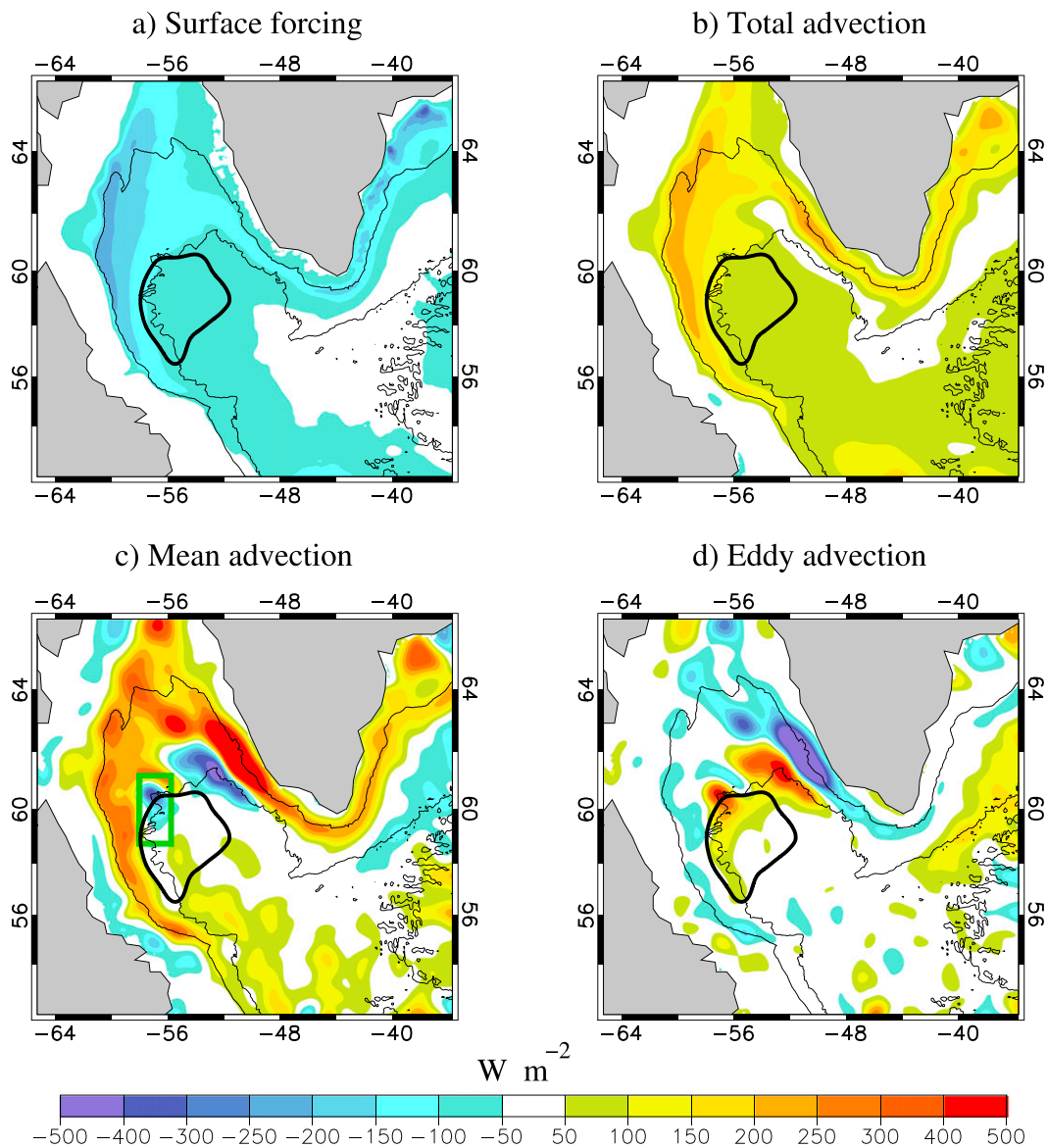


FIG. 7. Depth-integrated terms of heat budget (W m^{-2}): (a) surface heat flux, (b) total advection (mean plus eddy), (c) mean advection, and (d) eddy advection. The contribution due to the temperature tendency is relatively small (not shown). Also displayed are (thin lines) the 1- and 3-km isobaths and (thick contour) the region inside of which the depth of the winter (January–March) mixed layer exceeds 1000 m. The original advective fields have been smoothed before plotting using a Gaussian weighting with 50-km e -folding length scale. The small green box in (c), above the 3-km isobath and inside (or close to) the region of deep mixing, indicates the area of large heat divergence by the time-mean circulation discussed in section 4b (see also Fig. 10a).

surface flux (SF) of buoyancy is dominated by the flux of heat, consistent with Schmitt et al. (1989). However, along the coast of Labrador, where the ratio of thermal to haline contributions to the buoyancy flux is close to one (Schmitt et al. 1989), there is a net buoyancy gain at the surface (Fig. 8a). Much like in the case of heat balance, in most places the surface flux is closely balanced by the net advective convergence of buoyancy (Fig. 8b).

Also similar to the heat flux, the largest loss of buoyancy at the surface is not collocated with the deepest MLD (Fig. 8a), but rather is found in the transition region that connects the West Greenland Current with Labrador Current (Fig. 1).

The advective buoyancy fluxes (Figs. 8c,d) have the structures that are even more complex than those in the corresponding fluxes of heat (Figs. 7c,d). In particular, in

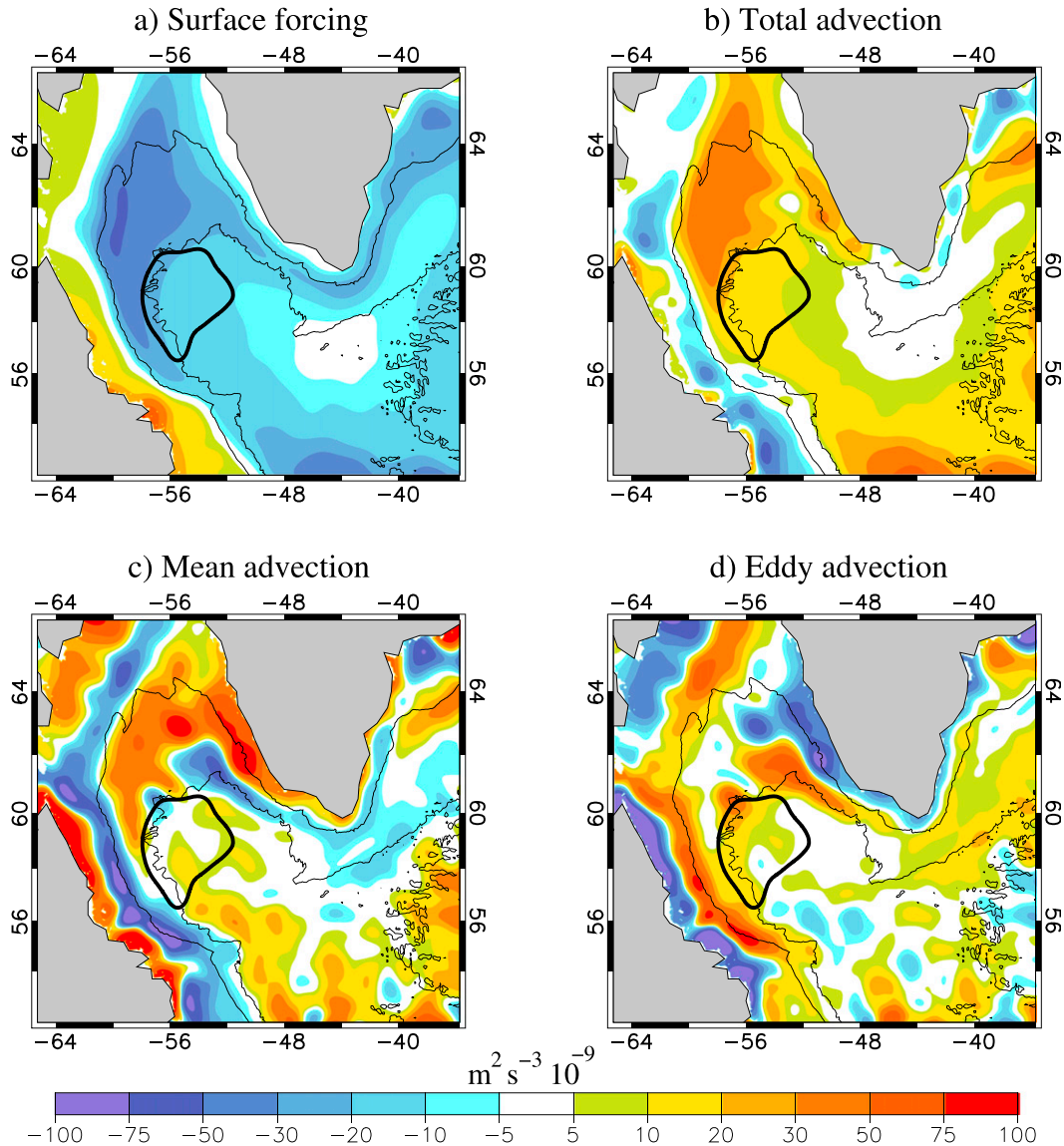


FIG. 8. Depth-integrated terms of buoyancy budget ($\text{m}^2 \text{s}^{-3} \times 10^{-9}$): (a) surface flux of buoyancy (computed after Gill 1982, p. 36), (b) total advection (mean plus eddy), (c) mean advection, and (d) eddy advection. Also displayed are (thin lines) the 1- and 3-km isobaths and (thick contour) the region inside of which the depth of winter (January–March) mixed layer exceeds 1000 m. The original fields have been smoothed before plotting using a Gaussian weighting with 50-km e -folding length scale.

addition to the large fluxes off the west coast of Greenland, there are also large advective buoyancy fluxes along the coast of Labrador, consistent with Kawasaki and Hasumi (2014). In the latter region, the model simulates a secondary maximum of EKE (Fig. 6a), which is also seen in observational estimates (e.g., Cuny et al. 2002; Lumpkin and Johnson 2013; R. Lumpkin 2013, personal communication) and in some other high-resolution model simulations (e.g., Chanut et al. 2008; Eden and Böning 2002). It has also been found that the freshwater that

exits from the Arctic Ocean through the Canadian Arctic Archipelago can strongly affect the balance of buoyancy along the coast of Labrador (Myers 2005; McGeehan and Maslowski 2011). In our model, eddies remove buoyancy from the coast and deposit it further offshore (Fig. 8d), not unlike in the model of McGeehan and Maslowski (2011). However, the largest eddy buoyancy convergence is found outside of the convective region, that is, along the 1-km isobath in the west, where strong density gradients exist all through

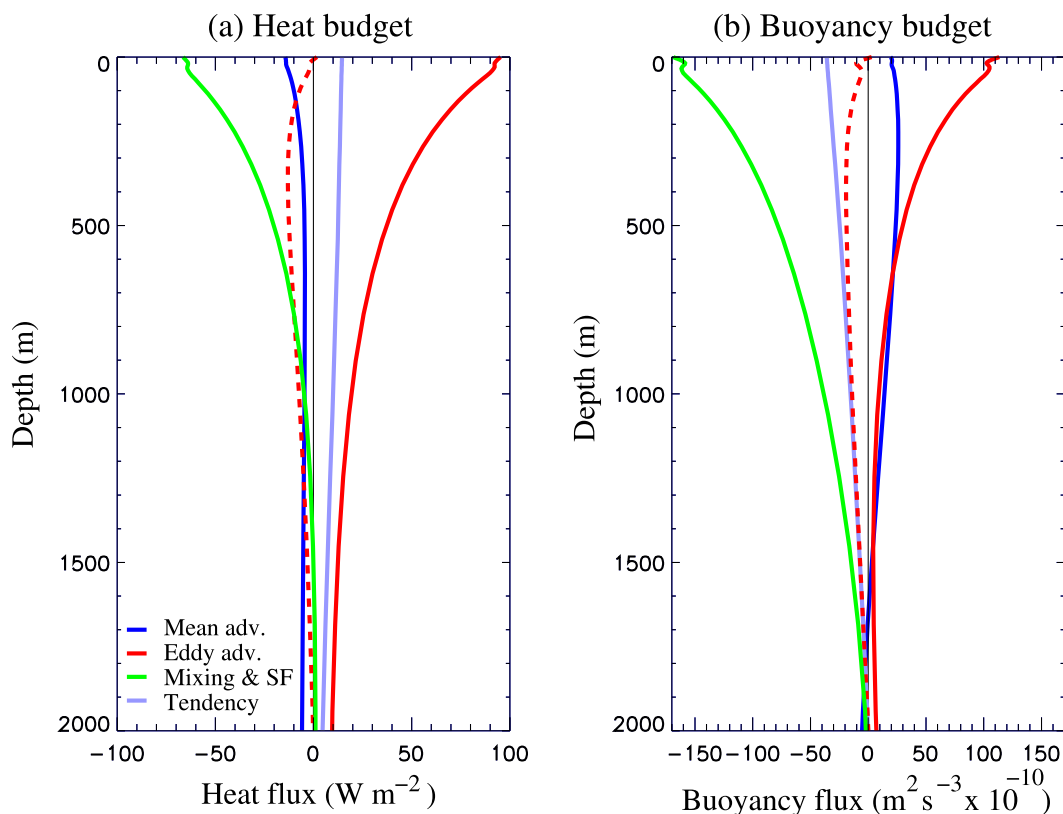


FIG. 9. Profiles of the integrated from the bottom different components of (a) heat and (b) buoyancy budgets (see section 4). The components are averaged over the region (A) where winter mixed layer depth exceeds 1000 m (see Fig. 3a): $A^{-1} \int_A \int_{-H}^z \mathcal{M} dA dz$ (mean adv.), $A^{-1} \int_A \int_{-H}^z \mathcal{E} dA dz$ (eddy adv.), and $A^{-1} \int_A \int_{-H}^z \mathcal{D} dA dz$ (mixing and SF) (see also section 4). Dashed curve represents a contribution of the upward eddy flux to the net eddy convergence of heat (or buoyancy). In the region, the mean winter σ_θ at 500, 1000, 1500, and 2000 m has, respectively, the following values: 27.796, 27.798, 27.801, and 27.808.

the water column (not shown). These eddy fluxes are largely compensated by the fluxes of buoyancy because of the local mean currents (Fig. 8c). The latter remove buoyancy along the 1-km isobath, which is a region of strong time-mean flow associated with the Labrador Current, and transport it closer to the coast of Labrador.

The depth-integrated budgets presented in Figs. 7 and 8 suggest that both eddies and mean currents can have a sizable contribution to the budgets of heat and buoyancy in the region of large MLDs, particularly along the 3-km isobath. We now take a closer look at this region.

b. Region of deep convection

Figure 9 displays the main components of heat and buoyancy budgets integrated from the bottom ($z = -H$) upward and averaged over the Labrador Sea area (A) where the winter MLD exceeds 1000 m (Fig. 3a); that is, $A^{-1} \int_A \int_{-H}^z \mathcal{M} dA dz$, and so on. In this region, \mathcal{D} largely

represents convection, except near the surface where it is dominated by the surface flux. Hence, it should be viewed accordingly: convection is expected to remove heat from the deeper ocean and deposit it to the upper ocean, where it can be lost to the atmosphere. In the region of deep convection, the loss of heat at the surface is expected to be larger than the heat transported to the upper layer by convection. Alternatively, one could say that in this region the surface heat loss is applied not only to the upper layer, but also to the layers below. The result is that more lateral heat flux has to come in to maintain the heat balance (Fig. 9; see also Figs. 7b and 8b). We shall discuss this more when considering the buoyancy budget terms in the upper Labrador Sea.

In the interior, the eddy convergence has contributions due to both lateral and vertical fluxes. The latter is given by $-\int_A \overline{w'c'} dA$ and, while relatively weak in the convective region (dashed curves in Figs. 9a,b), it is not negligible. Physically, the vertical eddy flux of buoyancy ($\overline{w'b'}$) represents a conversion of EPE to EKE. As

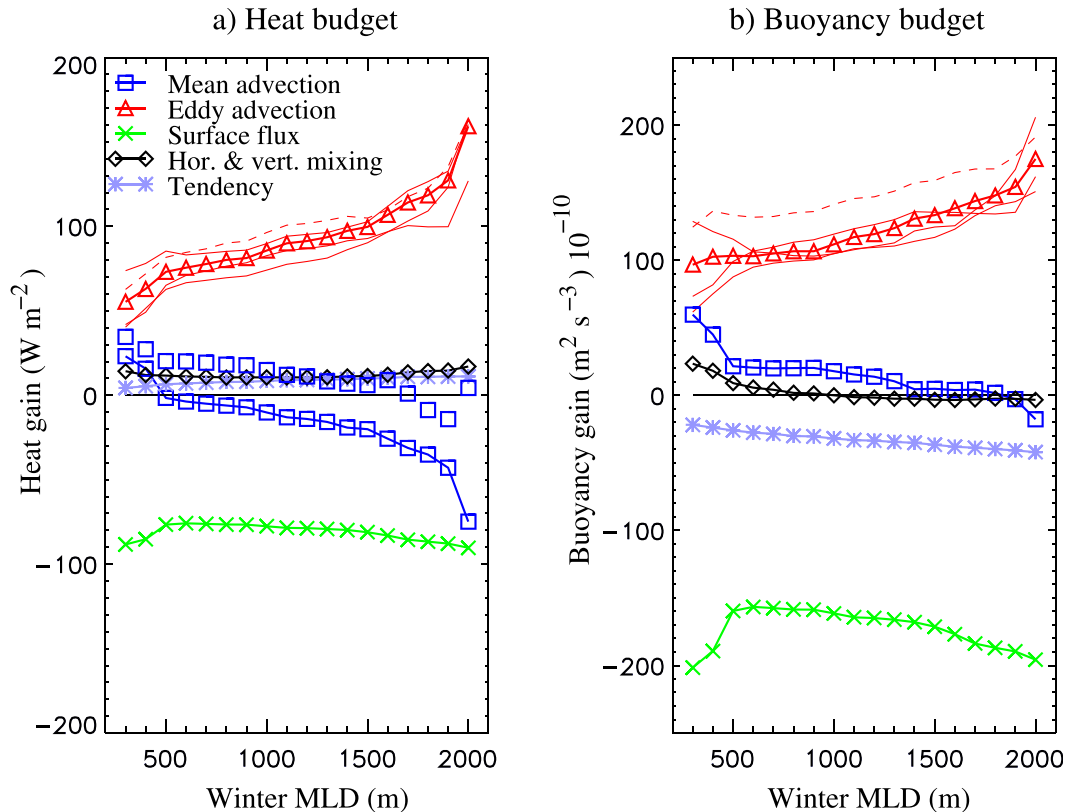


FIG. 10. Main components of (a) heat (W m^{-2}) and (b) buoyancy ($\text{m}^2 \text{s}^{-3} \times 10^{-10}$) budgets, integrated vertically over the cone-shaped winter MLD (see Fig. 3a) and averaged over the regions where the MLD exceeds the indicated values. Thin red curves represent eddy advection for different seasons, with dashed curve corresponding to spring (April–June). Note that the time-mean eddy flux does not have to be equal to the mean of the four seasons. In (a), the disconnected blue squares indicate the contribution of mean advection when the region indicated with the green box in Fig. 7c is excluded from the calculation.

expected, it is directed upward (i.e., $-\int_A \overline{w'b'} dA < 0$; i.e., eddies, on average, tend to remove potential energy). Thus, at any particular depth, the vertical eddy flux makes the ocean below that depth colder (less buoyant) and that above it warmer (more buoyant). The largest convergence of heat due to the upward component of eddy flux, as follows from its vertical structure (Fig. 9), is in the upper several hundred meters of the ocean. The spatial structure of the vertical eddy flux is discussed in the next subsection.

Chanut et al. (2008) present budgets of heat for several subregions, including for a circular region in the Labrador Sea interior (their Table 2). For the latter they find, consistent with our results (Fig. 9a), that the main balance is between the heat supplied by eddies and its removal by surface flux, with a smaller contribution due to mean advection. Here, rather than choosing a specific shape for our regions of interest, we consider the budget terms inside of the regions bounded by the contours of constant MLD (Fig. 3a). In addition, we consider not

only the budget of heat but also buoyancy. Finally, rather than integrating vertically through the whole water column, we integrate from the surface to the bottom of the winter MLD, that is, over the cone-shaped MLD domain (Fig. 3a), although integrating to the ocean bottom does not change substantially the presented budgets.

Figure 10 displays mean budgets of heat and buoyancy as functions of the MLD. The main balance, again, is between the eddy heat/buoyancy convergence and surface heat/buoyancy loss. However, there are interesting deviations from this balance. In particular, the eddy convergence increases with the increase of MLD, which is partly because of the increasing thickness of the mixed layer. Indeed, integrating from the surface to a fixed level (e.g., 400 m), rather than to the bottom of mixed layer, gives a more uniform eddy convergence. Still, however, it is a challenge to separate which of the three eddy types contributes most to this process, since each of them has the potential to do so. Indeed, CEs can become

stronger with an abrupt increase of MLD (Visbeck et al. 1996; Jones and Marshall 1997), such as in the western part of the domain (Fig. 3a). With the simulated mean background stratification of $N_{bg} = 1.02 \times 10^{-3} \text{ s}^{-1}$, and with the radius and maximum depth of the cone-shaped convection region of, respectively, 2×10^5 and 2×10^3 m (Fig. 3b), the time scale of restratification due to CEs is 0.91 yr [using Eq. (6) in Gelderloos et al. (2011) and their estimated value of 0.02 for the coefficient of eddy mixing efficiency].

However, the activity of CEs should be expected to decrease substantially a few months after convection, whereas the eddy convergence is not much different during spring than during the other seasons (Fig. 10). Instead, with the regions of progressively deeper MLDs simulated closer to the boundary current system (Fig. 3a), one may argue in favor of stronger BCEs contribution. With the model boundary current stratification of $N_{bc} = 1.72 \times 10^{-3} \text{ s}^{-1}$, the time scale of restratification because of the combination of CEs and BCEs is 0.65 yr, using Eq. (8) in Gelderloos et al. (2011) and the observed value for parameter ε of 0.1 in their Eq. (A2) [while we did not attempt to estimate the latter parameter using our model, we note that setting $\varepsilon = 0.05$, such as in Gelderloos et al. (2011), increases this restratification time scale from 0.65 to 0.76 yr]. Given that the model background stratification is only $2/3$ of the observed value, whereas the boundary current stratification is essentially correct, the model BCEs are probably more efficient in restratifying the water column than they are in reality. Finally, IRs also contribute. According to altimeter observations (Lilly et al. 2003), the majority of IRs take a southward pathway. [It should be noted that it is not clear yet whether IRs' activity is related to the convection activity, although Lilly et al. (2003) found more IRs in the early 2000s after almost a decade of deep convection.] If, however, some of the IRs were to take a rapid route along the 3-km isobath, such as discussed by Rykova et al. (2009), observed by Hátún et al. (2007) and simulated by our model (Fig. 6a), it would take them only several months to reach the deep convection area (given a typical translation speed of 0.15 m s^{-1} ; e.g., Hátún et al. 2007). While the total number of IRs generated in the model per year is roughly 15, less than half of them actually reach the convective area and some weaken significantly. Using 7 as the upper limit, and the model values for N_{bg} and N_{bc} , the time scale of restratification due to IRs is 1.52 yr [based on Eq. (10) in Gelderloos et al. (2011)]. The corresponding estimate for the combined effect of all three eddy types then is about 5.4 months, based on Eq. (12) in Gelderloos et al. (2011); with $\varepsilon = 0.05$, it increases to 6.1 months.

The increase in eddy convergence can be balanced both by surface flux and mean advection. The latter becomes particularly large in the case of heat budget, whereas the surface heat flux is less affected (Fig. 10a). Essentially, the heat divergence due to mean flows increases in the region of deepest MLD. However, the cooling due to the mean advection is mostly confined to the uppermost 400 m (Fig. 9a) and to a localized boundary region of deep mixing above the 3-km isobath (Fig. 7c). The mean temperature of this region is considerably warmer than in the interior, with colder water entering the upper part of it from below and warmer water leaving through the sides. Eliminating this region from the calculation leads to a much reduced cooling due to the mean advection (Fig. 10a; disconnected blue squares). The net effect of advection (mean plus eddy) is to warm up the Labrador Sea (Fig. 7b), which is balanced by the cooling at the surface (Fig. 7a).

Using the data from Lagrangian floats and making a realistic assumption about the mean temperature gradient in the region, Palter et al. (2008) estimate $\bar{\mathbf{u}} \cdot \nabla \theta$, or the rate with which mean horizontal advection can cool the boundary current, to be approximately 0.4 K yr^{-1} (or about 0.05 W m^{-2}). Assuming that most of this cooling is confined to the upper 400 m, such as in the model (Fig. 9a), gives 20 W m^{-2} . This is consistent with the rate of mean advective cooling that we obtain for the localized boundary region of deep mixing (Figs. 10a, 7c). We note, however, that Palter et al. (2008) calculated the mean advective heat flux across the 3-km isobath, which is not quite the same as advection by the mean flow.

The advection of buoyancy by the mean currents is relatively small in the regions where $\text{MLD} > 500 \text{ m}$ (Fig. 10b). This implies that the mean flows tend to follow mean isopycnals and that there is a compensation because of the freshwater effects. The water that does enter the region of deep winter mixed layers with the mean flows, leaves it largely on the same isopycnal. It therefore follows (Fig. 10) that the balance wherein the lateral eddy flux of C through the sides of the deepest MLD region compensates for the surface flux inside of the region (e.g., Jones and Marshall 1997) that holds more accurately when $C = b$ than when $C = \theta$. It should, however, be noted that the magnitude of the tendency term in the buoyancy budget, Fig. 10b, is quite large, reflecting the already discussed salinity drift.

c. Role of upward eddy flux

We now take a closer look at the spatial structure of advective buoyancy convergence in the upper Labrador Sea (Fig. 11) and, in particular, at the upward eddy flux. In the region of deep convection, the eddy impact on the

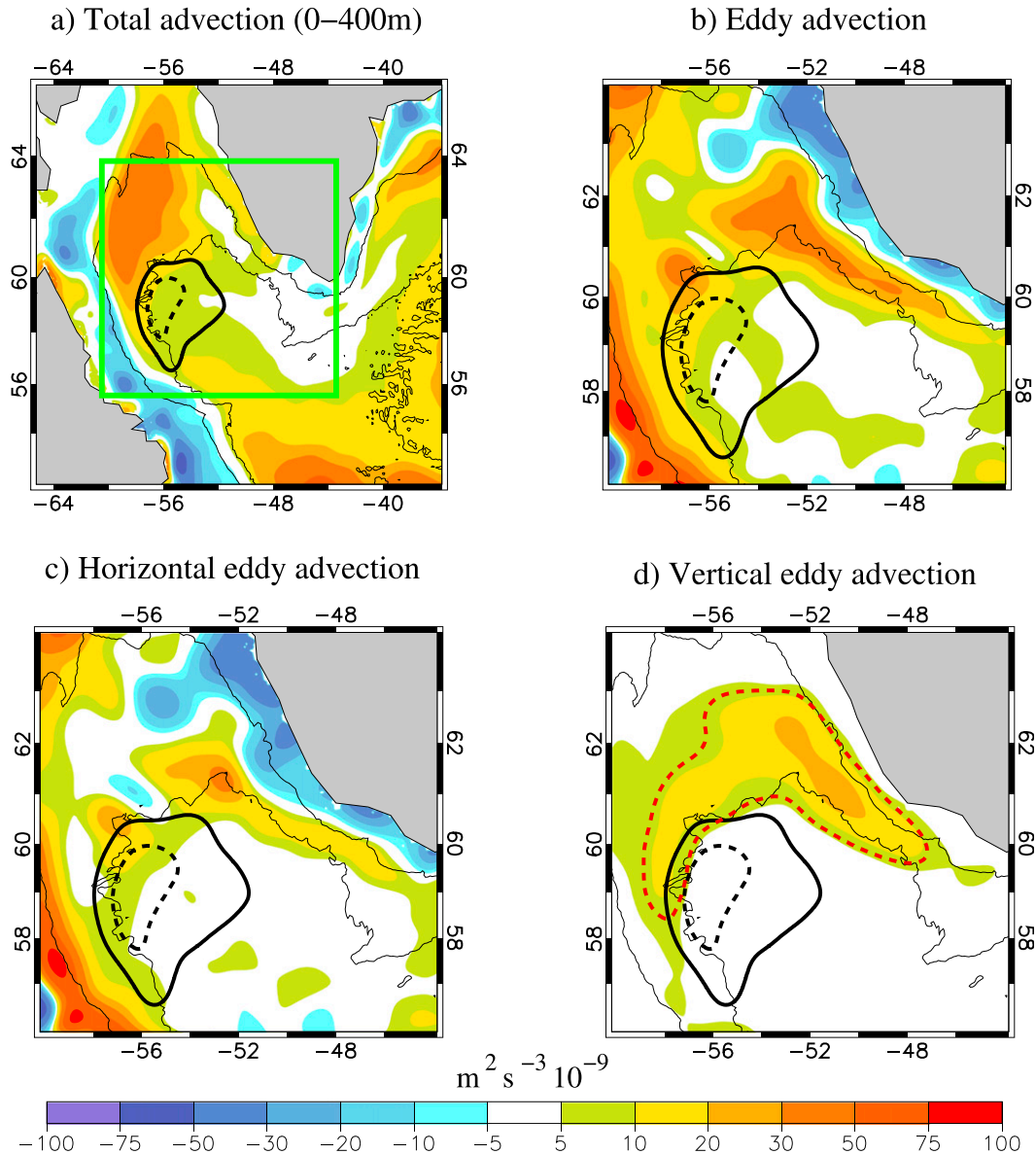


FIG. 11. Buoyancy budget terms ($\text{m}^2 \text{s}^{-3} \times 10^{-9}$) integrated over the upper ~ 400 m and shown (a) for the whole Labrador Sea and (b)–(d) for the subregion indicated in (a) with green box. The terms represent (a) total advection (mean, eddy, horizontal and vertical), (b) eddy advection (horizontal and vertical), (c) horizontal eddy advection, and (d) vertical eddy advection. The original fields have been smoothed before plotting using a Gaussian weighting with 50 km e -folding length scale. Shown with dashed red contour in (d) is the region where the upward eddy heat flux ($\rho_0 c_p w' \theta'$) across 400-m level exceeds 50 W m^{-2} . Also displayed are (thick black contours) the regions inside of which the depth of winter (January–March) mixed layer exceeds (solid) 1000 and (dashed) 1700 m, as well as (thin lines) the 1- and 3-km isobaths.

rate of buoyancy change is largest in the westernmost portion (Fig. 11b). This is where the buoyancy flux associated with BCEs may be expected to be large (e.g., McGeehan and Maslowski 2011), since the model simulates the deepest convection patch close to the boundary currents in the west. Indeed, in this region the eddy buoyancy convergence in Fig. 11b is likely to be largely

influenced by the BCEs. It is also the case that the sharp deepening of the mixed layer in the west (see Fig. 3a) creates strong lateral density gradients and favorable conditions for postconvective restratification by the CE during convection and shortly after it (e.g., Jones and Marshall 1997). In addition, the eddy buoyancy convergence is large along the 3-km isobath just north and

northeast of the convective region (Fig. 11b). In this region, the density gradients are much weaker than along the coast of Greenland farther north. This suggests that IRs also play an important part in supplying buoyant water into the Labrador Sea interior, thereby contributing to the restratification and confining the deep convection to a small region (e.g., Hátún et al. 2007). Such a remote impact of eddies would be difficult to represent in low-resolution models, as we shall see in section 5.

The budget of buoyancy in the upper Labrador Sea helps to explain the role of upward eddy flux $\overline{w'b'}$. In particular, in the region of deep convection most of the buoyancy is carried in by lateral eddy fluxes (Figs. 9b, 11b,c). In contrast, in the broad area to the north (north of 60°N in Fig. 11c), the integrated effect of the lateral component of eddy buoyancy convergence (or eddy flux at the region's boundary) is relatively small. This is because large positive and negative lateral eddy fluxes tend to cancel each other (by removing buoyant water from the coast of Greenland and depositing it farther offshore; Fig. 11c). As a result, the eddy buoyancy convergence into the upper 400-m water of the Labrador Sea north of 60°N is largely due to $\overline{w'b'}$ across the 400-m level² (Fig. 11d). The same applies to the heat flux (Fig. 11d); averaged between 60° and 64°N and 44° and 60°W, the upward eddy heat flux ($\rho_0 c_p \overline{w'\theta'}$) across the 400-m level is about 70 W m⁻² (this level is where the upward eddy heat flux is largest). This heat flux accounts for almost half of the net heat loss to the atmosphere in the region, with the other half supplied by the mean currents. Note that this region contains the area of strongest surface heat loss (Fig. 7a). Thus, by transporting heat to the near-surface ocean, the upward eddy heat flux plays an important part in the air–sea interaction in the northern part of the Labrador Sea. In addition, the upward eddy flux supplies buoyancy to the western and northwestern boundaries of the convective region (Fig. 11d), thereby affecting the deep convection indirectly.

Most of the upward eddy flux in the Labrador Sea is, apparently, associated with the generation of IRs off the west coast of Greenland, followed by conversion of their EPE into EKE (cf. Fig. 6a and Fig. 11d). An indication about the nature of the corresponding instability mechanism can be obtained by considering the rates of energy transfer associated with baroclinic (T_2) and barotropic (T_4) instabilities (using the notations

employed in several other studies; e.g., Beckmann et al. 1994; Eden and Böning 2002; Luo et al. 2011). These rates are given by

$$T_2 = -\tilde{N}^{-2}(\overline{u'b'\partial_x b} + \overline{v'b'\partial_y b}), \quad \text{and} \quad (4)$$

$$T_4 = -(\overline{u'u'\partial_x \bar{u}} + \overline{u'v'(\partial_x \bar{v} + \partial_y \bar{u})} + \overline{v'v'\partial_y \bar{v}}), \quad (5)$$

where \tilde{N} is the buoyancy frequency of horizontally averaged density. Physically, T_2 represents the conversion from mean potential to eddy potential energy and is an indicator of baroclinic instability; it can be shown that it enters the equation for buoyancy variance (b')², or EPE, as a source term. In turn, T_4 represents the conversion from mean kinetic to eddy kinetic energy; it is a source term in the equation for EKE and is an indicator of barotropic instability.

Using vertically averaged fields of T_2 and T_4 , Luo et al. (2011) found that it is the baroclinic instability mechanism that dominates the eddy generation process off the west coast of Greenland in their model. It should, however, be noted that while Luo et al. (2011) constrained T_2 and T_4 to be positive in their Fig. 7, these fields do have both positive and negative values in their model (H. Luo 2014, personal communication). In contrast, Eden and Böning (2002) argue in favor of barotropic instability in the region, even though their T_4 also has both positive and negative values (see their Fig. 13a).

In our model, the instability process appears to be dominated by baroclinic instability (Fig. 12). In particular, while T_2 is mostly positive in the region, and its structure broadly follows the structure of enhanced EKE (Fig. 12a), T_4 is mostly negative where EKE is large, but has very large positive values upstream (Fig. 12b), particularly in the region where geostrophic contours begin to converge. This is consistent with Eden and Böning (2002). Overall, T_4 has a more nonuniform structure than T_2 , with large positive and negative values cancelling each other when averaged over a broad area. However, for the subregion considered by Eden and Böning (2002), between 48° and 52°W, the barotropic energy transfer is large and positive, thereby increasing EKE. In contrast, negative regions of T_4 represent a conversion of EKE to KE of mean circulation. This indicates that some eddies are “recaptured” by the boundary current and reinforce it—another process that would be difficult to represent in low-resolution ocean models; this is discussed next.

5. Parameterized eddies

As noted in the introduction, observations reveal complex and rich dynamics of the Labrador Sea, characterized

²We note that, because the model employs a linear free-surface approximation, the vertical eddy flux does not vanish at the surface, although it is small.

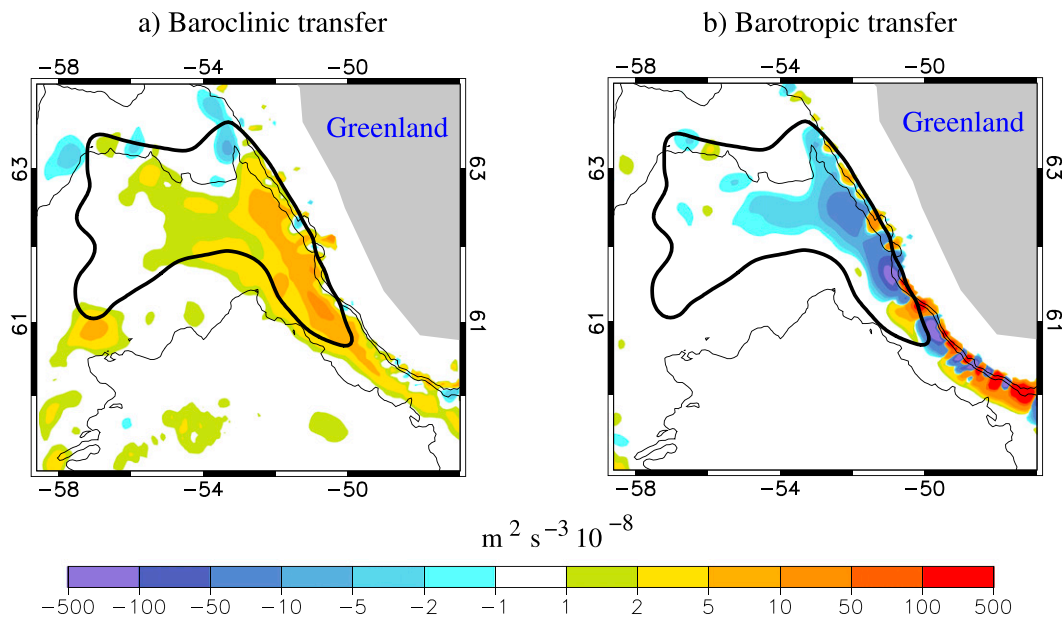


FIG. 12. Energy transfer (color; $\text{m}^2 \text{s}^{-3} \times 10^{-8}$) (a) from mean potential energy to eddy potential energy (associated with baroclinic instability) and (b) from mean kinetic energy to eddy kinetic energy (associated with barotropic instability), both averaged vertically from 200- to 1000-m depth. The thick contour represents the region inside of which the eddy kinetic energy at 55 m exceeds $100 \text{ cm}^2 \text{ s}^{-2}$. Also displayed (thin lines) are the 1-, 2-, and 3-km isobaths, as resolved by the $1/12^\circ$ model bathymetry.

by narrow boundary currents and countercurrents (e.g., Lavender et al. 2000; Cuny et al. 2002), nonuniform eddy activity (e.g., White and Heywood 1995; Lilly et al. 2003), and localized deep convection (Clarke and Gascard 1983; Pickart et al. 2002; Yashayaev and Loder 2009). This makes it difficult to simulate even the major components of the Labrador Sea dynamics and buoyancy budget using low-resolution ocean climate models, such as those employed for ocean and climate projections under global warming scenarios. One important component of the Labrador Sea buoyancy budget is related to the removal of buoyancy by eddies along the boundary currents (e.g., Spall 2004; Straneo 2006; Chanut et al. 2008; see also section 4). Here, we aim to use a low-resolution model with parameterized eddies and compare the associated eddy buoyancy convergence to the corresponding field simulated by the high-resolution model employed in the previous sections (note that comparing eddy buoyancy convergence automatically removes the rotational component of eddy fluxes). In addition, we test the sensitivity of the fluxes due to parameterized eddies to the atmospheric forcing, including to its frequency. Such a sensitivity may be expected through, for example, the impact of the forcing on the boundary current system.

For this, we use a low-resolution version of NEMO (ORCA1; see section 2) where the eddy buoyancy

convergence is represented by eddy-induced advection (GM90; Gent et al. 1995; see also the appendix). The GM90 parameterization, which is currently employed in most low-resolution ocean climate models, mimics a removal of potential energy by eddies from mean baroclinic currents. As such, it would not capture the generation of eddies due to barotropic instability. The latter likely contributes a significant part to the enhanced eddy activity off the southwest coast of Greenland (Eden and Böning 2002; Chanut et al. 2008; see also section 4). In addition, the GM90 parameterization assumes that eddy buoyancy flux is directed along mean buoyancy surfaces in the ocean interior. As a result, the implied vertical eddy buoyancy flux can be directed only upward, with a strength proportional to the local slope of mean isopycnals (see the appendix). It therefore does not parameterize nonlocal eddy effects, such as strong upward eddy buoyancy fluxes in the Labrador Sea interior simulated by the $1/12^\circ$ model (Fig. 11d). Indeed, away from the boundary currents the upward eddy buoyancy flux implied by the GM90 parameterization is two orders of magnitude weaker in the 1° models (not shown) than in the $1/12^\circ$ model. Nevertheless, this parameterization should capture the overall structure of eddy buoyancy transports along the (baroclinic) boundary currents in 1° models. Furthermore, Deacu and Myers (2005) show that the GM90 parameterization,

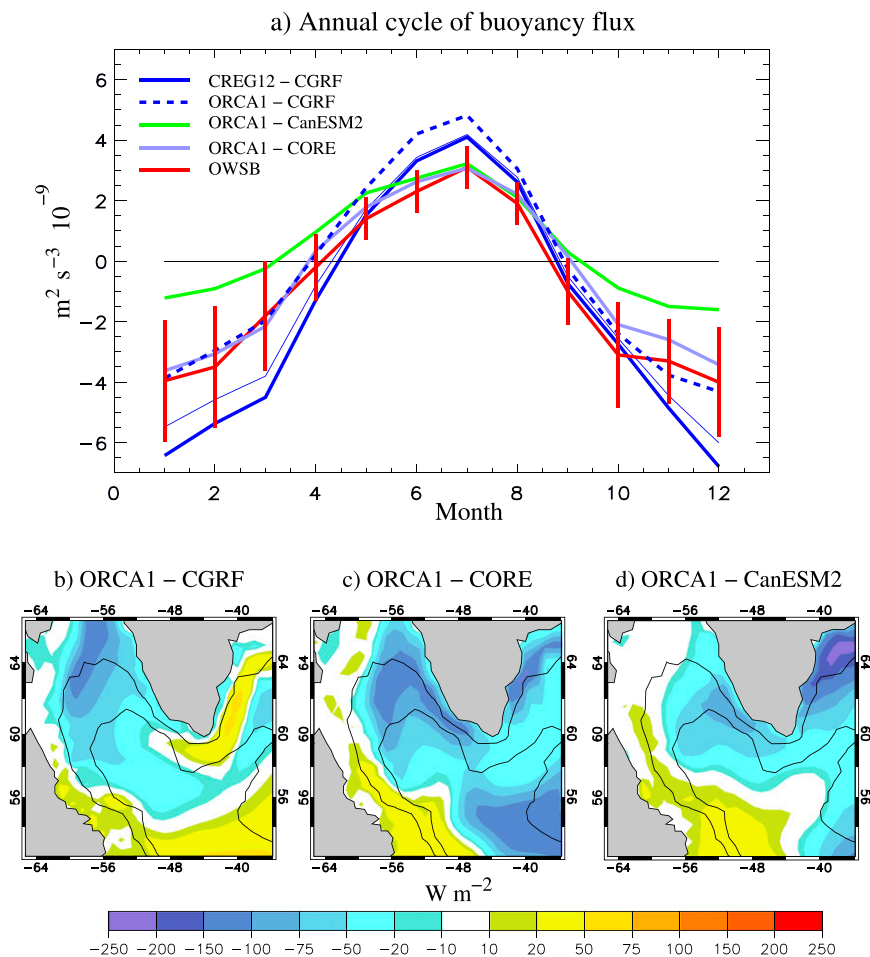


FIG. 13. (a) Mean annual cycle of buoyancy flux, simulated by the models and averaged over the green box in Fig. 11a and for each month. Also displayed is the mean (1949–73) buoyancy flux observed at OWSB (which was located at 56°N and 51°W) from Sathiyamoorthy and Moore (2002), with the vertical bars representing 1 standard deviation. The thin blue curve represents the same (CREG12-CGRF) model simulation as the thick blue curve, except the area of large buoyancy loss north of 60°N and west of 55°W (Fig. 8a) is excluded from the averaging. Mean heat flux in the (b) ORCA1-CGRF, (c) ORCA1-CORE, and (d) ORCA1-CanESM2 model simulations; also displayed are (thin lines) the 1- and 3-km isobaths.

with a formulation for the variable eddy transfer coefficient not unlike that employed here, can lead to improvements even in models with resolution of $1/3^\circ$.

The NEMO ORCA1 model is forced with several atmospheric products (see section 2). The corresponding mean annual cycles of surface buoyancy flux, averaged over a broad region of the Labrador Sea, are displayed in Fig. 13a. Compared to the high-resolution model, the low-resolution model tends to simulate weaker buoyancy loss in winter and fall, regardless of the atmospheric forcing product. This particularly applies to ORCA1-CanESM2, that is, when ORCA1 is forced with atmospheric fields from a fully coupled model, in which case the annual buoyancy gain at the

surface considerably exceeds the loss. Still, the monthly fluxes averaged over the large area are either within, or not too far beyond, the uncertainty of the (limited) observations. Note that while the observational climatology and standard deviations presented in Fig. 13a are based on 24 yr of point measurements at Ocean Weather Station Bravo (OWSB) (which was located at 56°N and 51°W and ended operation in 1974), unlike reanalysis products the corresponding data represent real observations.

However, the spatial structure of the surface fluxes is quite different between the ORCA1 model simulations (Figs. 13b–d) and from the CREG12 simulation (Fig. 7a). Furthermore, the structure of the net surface

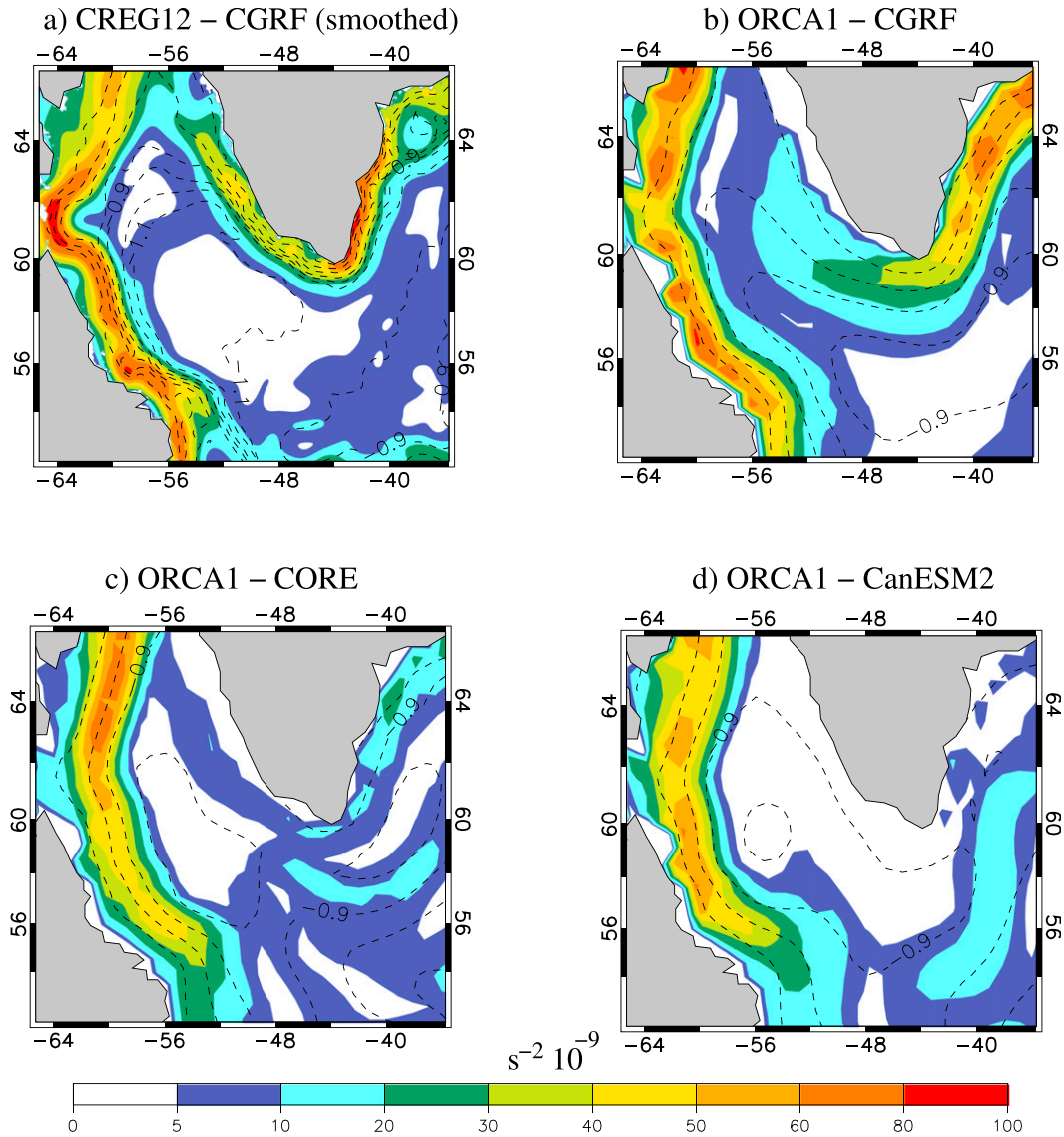


FIG. 14. Baroclinicity ($|\nabla\bar{b}|$; color; $s^{-2} \times 10^{-9}$) at 155-m depth simulated by the (a) CREG12-CGRF, (b) ORCA1-CGRF, (c) ORCA1-CORE, and (d) ORCA1-CanESM2. In the case of the $1/12^\circ$ model [in (a)], the original $|\nabla\bar{b}|$ field has been smoothed before plotting using a Gaussian weighting with 50-km e -folding length scale. Also displayed (dashed contours) are the time-mean sea surface heights (SSH) simulated by the corresponding models (contour interval -0.1 m).

heat flux in our $1/12^\circ$ model forced with CGRF data (Fig. 7a) has more in common with the net surface flux in Chanut et al. (2008, their Fig. 17a), who forced their model with ECMWF-based data, than with the surface flux in our 1° model forced with CGRF data (Fig. 13b). This illustrates that, locally, the net surface heat flux (and this is what actually is seen by ocean circulation) can be much more sensitive to model resolution (i.e., to the representation of ocean currents and associated advective heat convergence) than to the atmospheric data source. In particular, all ORCA1 runs, including

the one forced with CGRF atmospheric forcing, generate quite large heat gain in the southern and/or southwestern part of the Labrador Sea. In addition, the ORCA1-CGRF simulation has a positive surface heat flux south and southeast of Greenland. In contrast, the high-resolution model has this heat supplied to the Labrador Sea with the mean currents (Figs. 7b,c). The ORCA1-CORE model, in turn, has a reasonably good mean annual cycle north of 55°N (Fig. 13a), but perhaps too strong heat loss in the southeastern part of the region (Fig. 13c). This could be because of the

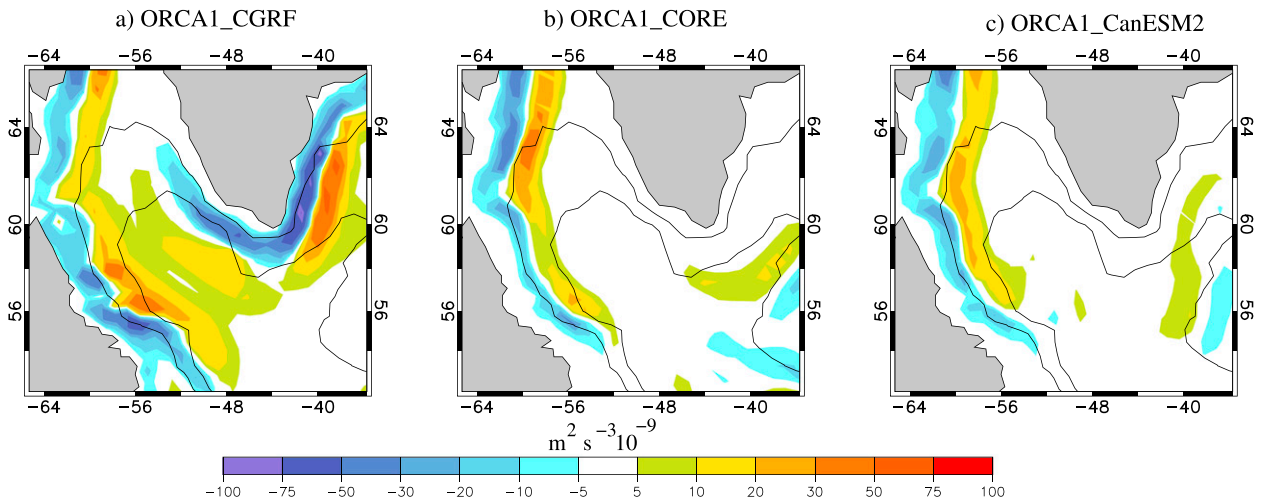


FIG. 15. Depth-integrated buoyancy convergence due to eddy-induced advection ($\text{m}^2 \text{s}^{-3} \times 10^{-9}$; color; see the [appendix](#)) in (a) ORCA1-CGRF, (b) ORCA1-CORE, and (c) ORCA1-CanESM2 (note that the equivalent quantity simulated by the $1/12^\circ$ model is shown in [Fig. 8d](#)). Also displayed are (thin lines) the 1- and 3-km isobaths, as resolved by the 1° model.

penetration of warm waters from the subtropics too far to the north. The ORCA1-CanESM2 simulation has a broad region of heat gain in the southwest and a strong heat loss outside of the Labrador Sea ([Fig. 13d](#)).

All ORCA1 runs simulate a reasonably strong baroclinicity (as given by $|\nabla \bar{b}|$) along the coast of Labrador ([Figs. 14b–d](#)). This is broadly consistent with the (smoothed) baroclinicity simulated by the high-resolution model ([Fig. 14a](#)). However, in the region off the west coast of Greenland, which is likely dominated by non-linear ocean dynamics, the baroclinicity is too weak in the ORCA1 simulations, particularly in ORCA1-CORE and ORCA1-CanESM2 ([Figs. 14c,d](#)). It is somewhat stronger in the ORCA1-CGRF model ([Fig. 14b](#)), but the corresponding boundary current is still too wide. As a result, the general structure of the eddy-induced buoyancy convergence in the ORCA1 simulations does resemble that in the CREG12 simulation along the coast of Labrador, but not along the coast of Greenland ([Fig. 15](#); compare to [Fig. 8d](#)). This particularly applies to ORCA1-CORE and ORCA1-CanESM2 runs ([Figs. 15b,c](#)). The parameterized eddies in the ORCA1-CGRF model do tend to remove buoyancy both along the coast of Greenland and Labrador and supply it somewhat farther offshore ([Fig. 15a](#)). However, while this is qualitatively in agreement with eddy-resolving models ([Fig. 8d](#); see also [Fig. 17d](#) in [Chanut et al. 2008](#)), as already noted much of this effect arises because the West Greenland Current is too wide in the 1° model ([Fig. 14b](#)).

To explore the sensitivity of this effect to forcing frequency, additional simulations were conducted

forcing the ORCA1 model with daily, 5-day, and monthly CGRF forcing. The corresponding buoyancy budgets for the central Labrador Sea are presented and compared to the high-resolution simulation in [Table 1](#). The lack of proper representation of eddy effects in the low-resolution model has a strong impact on the budgets. The supply of buoyancy to the Labrador Sea interior by the parameterized eddies is too weak, although it increases with the forcing frequency. However, while the strongest sensitivity to the forcing frequency is found off the coast of Greenland ([Fig. 16](#)), the associated baroclinicity penetrates too far into the Labrador Sea interior (cf. [Fig. 14a](#) and [Fig. 14b](#)). As such, the corresponding increase of eddy buoyancy convergence in the interior is due to local, rather than remote, eddy effects.

6. Discussion and conclusions

While the Labrador Sea is not the most eddy-active region in the World Ocean, eddies nonetheless play a key role in its budget of heat. This particularly applies to a localized region in the western part of the sea where deep mixing can penetrate to large depths in winter, contributing to the global ocean ventilation. The associated subsurface-to-surface heat transfer, if disrupted for a long period of time (by, e.g., a large enough buoyancy anomaly) could have a major impact on the climate.

To obtain further insight on the role of eddies in the Labrador Sea budgets of heat and buoyancy, we use a high-resolution ($1/12^\circ$) ocean model forced with high-resolution (33 km, 3 h) atmospheric fields. The simulated Labrador Sea circulation, distribution of EKE, winter MLD, and water mass properties show many

TABLE 1. Components of the mean budget of buoyancy ($\text{m}^2\text{s}^{-3} \times 10^{-10}$) in the Labrador Sea interior, roughly between 57° and 60°N and 52° and 56°W , corresponding to the 1° model (with different frequencies of atmospheric forcing) and to the $1/12^\circ$ model. The “residual” term includes the trend, horizontal dissipation (if applicable), and effects arising because of nonlinearities of the equation of state. Positive values indicate buoyancy gain.

Resolution (forcing freq.)	Mean adv.	Eddy adv.	Surface flux	Residual
1° (month)	18.6	34.0	-61.2	-8.6
1° (5 days)	32.9	47.0	-74.6	5.3
1° (1 day)	29.5	52.6	-70.7	11.4
1° (3 h)	22.7	87.4	-93.3	16.8
$1/12^\circ$ (3 h)	20.5	122.6	-161.4	-18.3

observed features. In general agreement with previous studies, it is found that eddies remove heat along the coast and supply it to the interior. However, this process is highly nonuniform. While the strongest eddy heat divergence is simulated off the west coast of Greenland,

the eddy buoyancy divergence is enhanced not only there, but also along the coast of Labrador. This is where observations and models show a secondary maximum in EKE and where low salinity water is supplied in the model through the Hudson/Baffin Bays.

It should also be noted that the presented results are more applicable to the time periods characterized by deep mixing, with at least some of it taking place close to the slope region in the west, around the 3-km isobath. An example of such a situation is the hydrographic cruise in the winter of 1997 (Pickart et al. 2002; Lavender et al. 2000). Furthermore, the locations of both the EKE maximum and deep mixing are simulated too far north, compared to observational estimates. It is important to keep this in mind, since the robustness of some of the presented results may depend on the relative position of deep mixing and the EKE maximum. In particular, we find that the convergence of heat and buoyancy by eddies significantly increases with the convective mixing

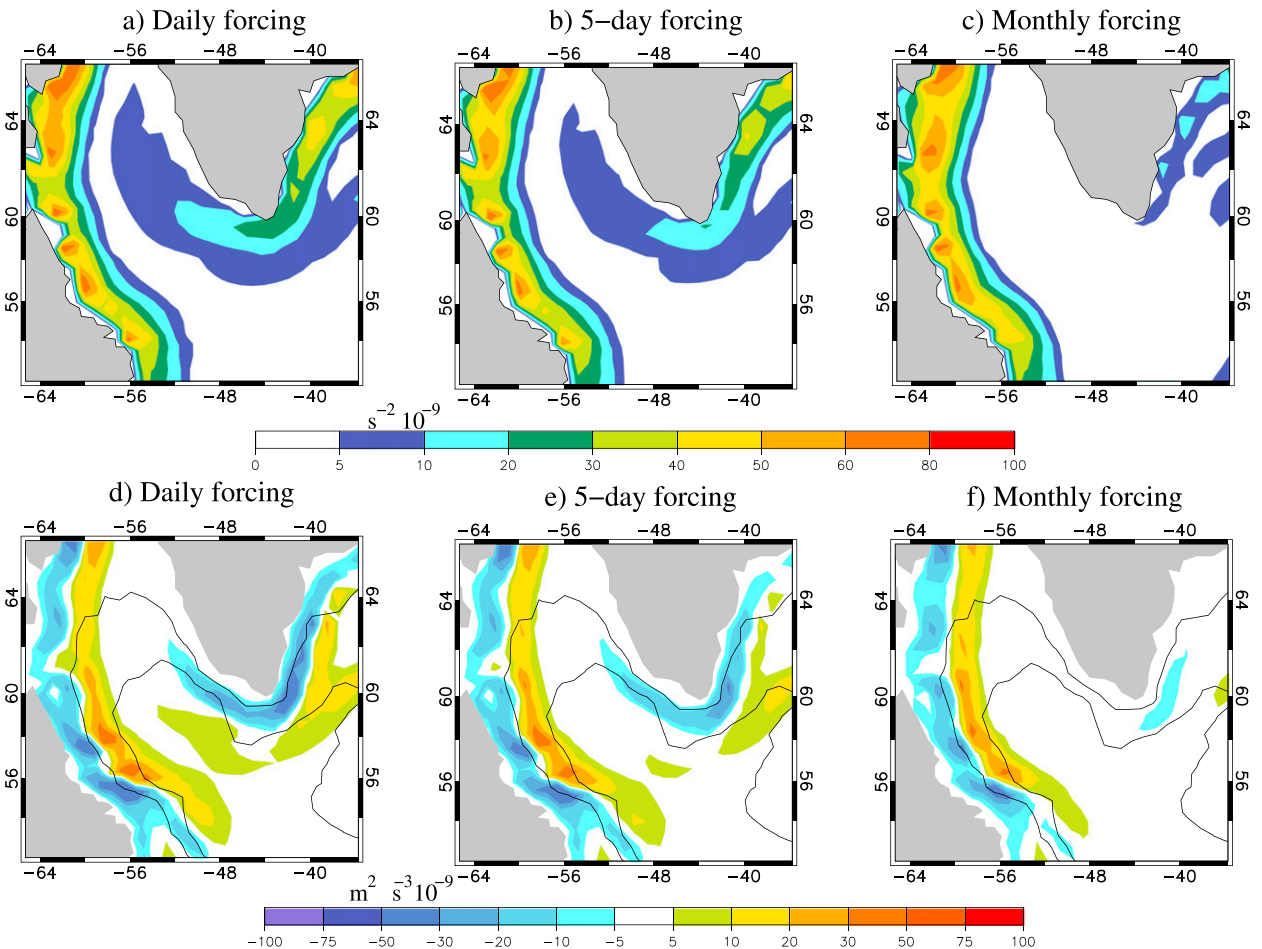


FIG. 16. (top) Baroclinicity ($|\bar{v}| \text{s}^{-2} \times 10^{-9}$) at 155-m depth and (bottom) depth-integrated buoyancy convergence due to eddy-induced advection ($\text{m}^2\text{s}^{-3} \times 10^{-9}$; see the appendix) simulated by the ORCA1 model forced with (a),(d) daily, (b),(e) 5-day, and (c),(f) monthly CGRF forcing. Also displayed in (d)–(f) are (thin lines) the 1- and 3-km isobaths, as resolved by the 1° model.

penetrating to deeper layers, which is in part due to the increased thickness of the convective patch. The divergence of heat by the time-mean circulation can play an important part in offsetting some of this eddy flux increase, but perhaps only in the boundary current region. In our $1/12^\circ$ model, this happens locally, along the 3-km isobath.

We also find that in the broad area to the north of the convective region, vertical eddy fluxes, associated with conversion of EPE to EKE, play an important part in the heat and buoyancy budgets of the upper Labrador Sea. In particular, the upward eddy heat flux across the 400-m depth level, averaged over a broad area north of 60°N , accounts for up to half of the net heat loss to the atmosphere in the region, with the other half supplied by the mean currents.

In addition to the high-resolution model, we also employ a low-resolution (1°) model. We address the question whether the structure of eddy buoyancy convergence, simulated by the $1/12^\circ$ model, could be, at least broadly, reproduced by parameterized eddies in the low-resolution model. It is found that the low-resolution model does capture the general structure of eddy buoyancy transport along the Labrador Current. However, while some improvements can be made by forcing it with the high-resolution atmospheric fields, the 1° model is deficient in the region off the west coast of Greenland. In this region, the boundary current simulated by the low-resolution model is too weak and wide. Furthermore, forcing the 1° model with observationally based atmospheric data (as opposite to the data derived from an unconstrained climate model) does not change this result. We therefore conclude that it may not be easy, if possible at all, to correctly represent the eddy-driven restratification of the Labrador Sea in low-resolution ocean climate models.

Acknowledgments. The authors thank Annalisa Bracco, Jérôme Chanut, Caroline Katsman, Hao Luo, and Rick Lumpkin for discussions and for answering many questions about their related studies. The first author also benefited from an exchange of emails with Peter Rhines, who at the early stage of this study provided links to important sources of observations in the Labrador Sea and to several insightful papers on the subject. We also thank Bill Merryfield, Neil Swart, and two anonymous reviewers for very constructive comments. The study is conducted as part of the Ventilation, Interactions and Transports across the Labrador Sea (VITALS) research project, funded by Natural Sciences and Engineering Research Council of Canada. We would like to acknowledge the Atlantic Zone Off-Shelf Monitoring Program (AZOMP) of Fisheries and Oceans Canada

(DFO) and Argo Program, which are part of the Global Climate Observing System, for providing their data. We also would like to thank the NEMO development team for providing the model and continuous guidance. ECMWF ERA-Interim product used in this study was obtained from the ECMWF data server. The WHOI ocean heat flux product was provided by the OAFflux project (<http://oafux.whoi.edu>) funded by the NOAA Climate Observations and Monitoring program. The gridded Archiving, Validation, and Interpretation of Satellite Oceanographic data (AVISO) near-surface geostrophic velocity was obtained online (from www.aviso.altimetry.fr/en/home.html).

APPENDIX

Eddy-Induced Transport of Buoyancy

It can be shown that a budget of buoyancy of the form

$$\partial_t \bar{b} + \bar{\mathbf{u}} \cdot \nabla \bar{b} + \bar{w} \partial_z \bar{b} + \nabla \cdot (\bar{\mathbf{u}}'b') + \partial_z (\bar{w}'b') = \mathcal{D} \quad (\text{A1})$$

can be written in the following equivalent form:

$$\partial_t \bar{b} + (\bar{\mathbf{u}} + \mathbf{u}^*) \cdot \nabla \bar{b} + (\bar{w} + w^*) \partial_z \bar{b} = \mathcal{D} - \partial_z G, \quad (\text{A2})$$

where the “eddy-induced” velocities are given by

$$\mathbf{u}^* = -\partial_z \left(\frac{\bar{\mathbf{u}}'b'}{\partial_z \bar{b}} \right), \quad w^* = \nabla \cdot \left(\frac{\bar{\mathbf{u}}'b'}{\partial_z \bar{b}} \right), \quad (\text{A3})$$

while G , which is a measure of deviation of the eddy buoyancy flux from being directed along mean buoyancy surface, is

$$G = \bar{w}'b' + \left(\frac{\bar{\mathbf{u}}'b' \cdot \nabla \bar{b}}{\partial_z \bar{b}} \right). \quad (\text{A4})$$

Assuming that the eddy buoyancy flux is directed along mean buoyancy surfaces (i.e., $G = 0$), and using a downgradient closure, $\bar{\mathbf{u}}'b' = -K\nabla \bar{b}$ (such as in the NEMO ORCA1 that we employ), one obtains locally for a stable stratification $w'b' = K(\nabla \bar{b}/N)^2 > 0$, where K is the eddy transfer coefficient (see section 2a) and all other notations are conventional.

REFERENCES

- Barnier, B., and Coauthors, 2007: Eddy-permitting ocean circulation hindcasts of past decades. *CLIVAR Exchanges*, No. 42, International CLIVAR Project Office, Southampton, United Kingdom, 8–10. [Available online at http://www.clivar.org/sites/default/files/documents/wgomd/core/Barnier_07.pdf.]

- Beckmann, A., C. W. Böning, B. Brugge, and D. Stammer, 1994: On the generation and role of eddy variability in the central North Atlantic Ocean. *J. Geophys. Res.*, **99**, 20381–20391, doi:10.1029/94JC01654.
- Blanke, B., and P. Delecluse, 1993: Variability of the tropical Atlantic Ocean simulated by a general circulation model with two different mixed-layer physics. *J. Phys. Oceanogr.*, **23**, 1363–1388, doi:10.1175/1520-0485(1993)023<1363:VOTTAO>2.0.CO;2.
- Chanut, J., B. Barnier, W. Large, L. Debreu, T. Penduff, J. M. Molines, and P. Mathiot, 2008: Mesoscale eddies in the Labrador Sea and their contribution to convection and restratification. *J. Phys. Oceanogr.*, **38**, 1617–1643, doi:10.1175/2008JPO3485.1.
- Clarke, R. A., and J.-C. Gascard, 1983: The formation of Labrador Sea Water. Part I: Large-scale processes. *J. Phys. Oceanogr.*, **13**, 1764–1778, doi:10.1175/1520-0485(1983)013<1764:TFOLSW>2.0.CO;2.
- Cuny, J., P. B. Rhines, P. P. Niiler, and S. Bacon, 2002: Labrador Sea boundary currents and the fate of the Irminger Sea Water. *J. Phys. Oceanogr.*, **32**, 627–647, doi:10.1175/1520-0485(2002)032<0627:LSBCAT>2.0.CO;2.
- Curry, R. G., M. S. McCartney, and T. M. Joyce, 1998: Oceanic transport of subpolar climate signals to mid-depths subtropical waters. *Nature*, **391**, 575–577, doi:10.1038/35356.
- Danabasoglu, G., and Coauthors, 2014: North Atlantic simulations in Coordinated Ocean-Ice Reference Experiments phase II (CORE-II). Part I: Mean states. *Ocean Modell.*, **73**, 76–107, doi:10.1016/j.ocemod.2013.10.005.
- Deacu, D., and P. G. Myers, 2005: Effect of a variable eddy transfer coefficient in an eddy-permitting model of the subpolar North Atlantic Ocean. *J. Phys. Oceanogr.*, **35**, 289–307, doi:10.1175/JPO-2674.1.
- Dee, D. P., and Coauthors, 2011: The ERA-Interim reanalysis: Configuration and performance of the data assimilation system. *Quart. J. Roy. Meteor. Soc.*, **137**, 553–597, doi:10.1002/qj.828.
- Dickson, R., J. Lazier, J. Meincke, P. Rhines, and J. Swift, 1996: Long-term coordinated changes in the convective activity of the North Atlantic. *Prog. Oceanogr.*, **38**, 241–295, doi:10.1016/S0079-6611(97)00002-5.
- Eady, E., 1949: Long waves and cyclone waves. *Tellus*, **1**, 33–52, doi:10.1111/j.2153-3490.1949.tb01265.x.
- Eden, C., and C. Böning, 2002: Sources of eddy kinetic energy in the Labrador Sea. *J. Phys. Oceanogr.*, **32**, 3346–3363, doi:10.1175/1520-0485(2002)032<3346:SOEKEI>2.0.CO;2.
- Gaspar, P., Y. Gregoris, and J. M. Lefevre, 1990: A simple eddy kinetic energy model for simulations of the oceanic vertical mixing: Tests at Station Papa and long-term upper ocean study site. *J. Geophys. Res.*, **95**, 16179–16193, doi:10.1029/JC095iC09p16179.
- Gelderloos, R., C. A. Katsman, and S. S. Drijfhout, 2011: Assessing the roles of three eddy types in restratifying the Labrador Sea after deep convection. *J. Phys. Oceanogr.*, **41**, 2102–2119, doi:10.1175/JPO-D-11-054.1.
- Gent, P. R., and J. C. McWilliams, 1990: Isopycnal mixing in ocean general circulation models. *J. Phys. Oceanogr.*, **20**, 150–155, doi:10.1175/1520-0485(1990)020<0150:IMIOCM>2.0.CO;2.
- , J. Willebrand, T. J. McDougall, and J. C. McWilliams, 1995: Parameterizing eddy-induced tracer transports in ocean circulation models. *J. Phys. Oceanogr.*, **25**, 463–474, doi:10.1175/1520-0485(1995)025<0463:PEITTI>2.0.CO;2.
- Gill, A. E., 1982: *Atmosphere–Ocean Dynamics*. Academic Press, 662 pp.
- Gnanadesikan, A., R. D. Slater, P. S. Swathi, and G. K. Vallis, 2005: The energetics of ocean heat transport. *J. Climate*, **18**, 2604–2616, doi:10.1175/JCLI3436.1.
- Griffies, S., and Coauthors, 2009: Coordinated Ocean-Ice Reference Experiments (COREs). *Ocean Modell.*, **26**, 1–46, doi:10.1016/j.ocemod.2008.08.007.
- Hátún, H., C. C. Eriksen, and P. B. Rhines, 2007: Buoyant eddies entering the Labrador Sea observed with gliders and altimetry. *J. Phys. Oceanogr.*, **37**, 2838–2854, doi:10.1175/2007JPO3567.1.
- Houghton, R. W., and M. H. Visbeck, 2002: Quasi-decadal salinity fluctuations in the Labrador Sea. *J. Phys. Oceanogr.*, **32**, 687–701, doi:10.1175/1520-0485(2002)032<0687:QDSFIT>2.0.CO;2.
- Jones, H., and J. Marshall, 1997: Restratification after deep convection. *J. Phys. Oceanogr.*, **27**, 2276–2287, doi:10.1175/1520-0485(1997)027<2276:RADC>2.0.CO;2.
- Katsman, C. A., M. A. Spall, and R. S. Pickart, 2004: Boundary current eddies and their role in the restratification of the Labrador Sea. *J. Phys. Oceanogr.*, **34**, 1967–1983, doi:10.1175/1520-0485(2004)034<1967:BCEATR>2.0.CO;2.
- Kawasaki, T., and H. Hasumi, 2014: Effect of freshwater from the West Greenland Current on the winter deep convection in the Labrador Sea. *Ocean Modell.*, **75**, 51–64, doi:10.1016/j.ocemod.2014.01.003.
- Large, W. G., and S. G. Yeager, 2009: Global climatology of an interannually varying air–sea flux data set. *Climate Dyn.*, **33**, 341–364, doi:10.1007/s00382-008-0441-3.
- Lavender, K., R. E. Davis, and W. B. Owens, 2000: Mid-depth recirculation observed in the interior Labrador and Irminger Seas by direct velocity measurements. *Nature*, **407**, 66–69, doi:10.1038/35024048.
- Lazier, J. R. N., R. S. Pickart, and P. B. Rhines, 2001: Deep convection in the Labrador Sea. *Ocean Circulation and Climate*, G. Siedler, J. Church, and J. Gould, Eds., International Geophysics Series, Vol. 77, Academic Press, 387–400.
- , R. Hendry, A. Clarke, I. Yashayaev, and P. Rhines, 2002: Convection and restratification in the Labrador Sea. *Deep-Sea Res. I*, **49**, 1819–1835, doi:10.1016/S0967-0637(02)00064-X.
- Le Galloudec, O., R. Bourdalle-Badie, Y. Drillet, C. Derval, and C. Bricaud, 2008: Simulation of meso-scale eddies in the Mercator Global Ocean High Resolution Model. *Mercator-Ocean Newsletter*, No. 31, Ramonville Saint-Agne, France, 22–30. [Available online at <http://www.mercator-ocean.fr/actualites-agenda/newsletter/newsletter-Newsletter-31-The-GODAE-project>.]
- Lilly, J. M., and P. B. Rhines, 2002: Coherent eddies in the Labrador Sea observed from a mooring. *J. Phys. Oceanogr.*, **32**, 585–598, doi:10.1175/1520-0485(2002)032<0585:CEITLS>2.0.CO;2.
- , —, M. Visbeck, R. Davis, J. R. N. Lazier, F. Schott, and D. Farmer, 1999: Observing deep convection in the Labrador Sea during winter 1994/95. *J. Phys. Oceanogr.*, **29**, 2065–2098, doi:10.1175/1520-0485(1999)029<2065:ODCITL>2.0.CO;2.
- , —, F. Schott, K. Lavender, J. Lazier, U. Send, and E. D’Asaro, 2003: Observations of the Labrador Sea eddy field. *Prog. Oceanogr.*, **59**, 75–176, doi:10.1016/j.pocan.2003.08.013.
- Lumpkin, R., and G. C. Johnson, 2013: Global ocean surface velocities from drifters: Mean, variance, El Niño–Southern Oscillation response, and seasonal cycle. *J. Geophys. Res.*, **118**, 2992–3006, doi:10.1002/jgrc.20210.

- Luo, H., A. Bracco, and E. Di Lorenzo, 2011: The interannual variability of the surface eddy kinetic energy in the Labrador Sea. *Prog. Oceanogr.*, **91**, 295–311, doi:10.1016/j.pocean.2011.01.006.
- Madec, G., 2008: NEMO ocean engine, version 3.0. Note du Pole de modélisation de l'Institut Pierre-Simon Laplace 27, 217 pp. [Available online at http://www.nemo-ocean.eu/content/download/5302/31828/file/NEMO_book.pdf.]
- , and Coauthors, 2012: NEMO ocean engine, version 3.4. Note du Pole de modélisation de l'Institut Pierre-Simon Laplace 27, 367 pp. [Available online at http://www.nemo-ocean.eu/content/download/21612/97924/file/NEMO_book_3_4.pdf.]
- Maximenko, N. A., and P. P. Niiler, 1999: Hybrid decade-mean global sea level with mesoscale resolution. *Recent Advances in Marine Science and Technology*, N. Saxena, Ed., PACON International, 55–59.
- McCartney, M. S., 1992: Recirculating components to the deep boundary current of the northern North Atlantic. *Prog. Oceanogr.*, **29**, 283–383, doi:10.1016/0079-6611(92)90006-1.
- McGeehan, T., and W. Maslowski, 2011: Impact of shelf-basin freshwater transport on deep convection in the western Labrador Sea. *J. Phys. Oceanogr.*, **41**, 2187–2210, doi:10.1175/JPO-D-11-01.1.
- Moore, G. W. K., R. S. Pickart, I. A. Renfrew, and K. Våge, 2014: What causes the location of the air-sea turbulent heat flux maximum over the Labrador Sea? *Geophys. Res. Lett.*, **41**, 3628–3635, doi:10.1002/2014GL059940.
- Myers, P. G., 2005: Impact of freshwater from the Canadian Arctic Archipelago on Labrador Sea Water formation. *Geophys. Res. Lett.*, **32**, L06605, doi:10.1029/2004GL022082.
- Palter, J. B., M. S. Lozier, and K. L. Lavender, 2008: How does Labrador Sea Water enter the deep western boundary current? *J. Phys. Oceanogr.*, **38**, 968–983, doi:10.1175/2007JPO3807.1.
- Pickart, R. S., M. A. Spall, and J. R. N. Lazier, 1997: Mid-depth ventilation in the western boundary current system of the sub-polar gyre. *Deep-Sea Res.*, **44**, 1025–1054, doi:10.1016/S0967-0637(96)00122-7.
- , D. J. Torres, and R. A. Clarke, 2002: Hydrography of the Labrador Sea during active convection. *J. Phys. Oceanogr.*, **32**, 428–457, doi:10.1175/1520-0485(2002)032<0428:HOTLSD>2.0.CO;2.
- Redi, M. H., 1982: Oceanic isopycnal mixing by coordinate rotation. *J. Phys. Oceanogr.*, **12**, 1154–1158, doi:10.1175/1520-0485(1982)012<1154:OIMBCR>2.0.CO;2.
- Rykova, T., F. Straneo, J. M. Lilly, and I. Yashayaev, 2009: Irminger Current anticyclones in the Labrador Sea observed in the hydrographic record, 1990–2004. *J. Mar. Res.*, **67**, 361–384, doi:10.1357/002224009789954739.
- Sathiyamoorthy, S., and G. W. K. Moore, 2002: Buoyancy flux at Ocean Weather Station Bravo. *J. Phys. Oceanogr.*, **32**, 458–474, doi:10.1175/1520-0485(2002)032<0458:BFAOWS>2.0.CO;2.
- Schmitt, R. W., P. S. Bogden, and C. E. Dorman, 1989: Evaporation minus precipitation and density fluxes for the North Atlantic. *J. Phys. Oceanogr.*, **19**, 1208–1221, doi:10.1175/1520-0485(1989)019<1208:EMPADF>2.0.CO;2.
- Smethie, W. M., Jr., R. A. Fine, A. Putzka, and E. P. Jones, 2000: Tracing the flow North Atlantic Deep Water using chlorofluorocarbons. *J. Geophys. Res.*, **105**, 14 297–14 323, doi:10.1029/1999JC900274.
- Smith, G. C., F. Roy, P. Mann, F. Dupont, B. Brasnett, J.-F. Lemieux, S. Larochea, and S. Belaira, 2013: A new atmospheric dataset for forcing ice–ocean models: Evaluation of reforecasts using the Canadian global deterministic prediction system. *Quart. J. Roy. Meteor. Soc.*, **140**, 881–894, doi:10.1002/qj.2194.
- Spall, M. A., 2004: Boundary currents and water mass transformation in marginal seas. *J. Phys. Oceanogr.*, **34**, 1197–1213, doi:10.1175/1520-0485(2004)034<1197:BCAWTI>2.0.CO;2.
- Straneo, F., 2006: Heat and freshwater transport through the central Labrador Sea. *J. Phys. Oceanogr.*, **36**, 606–628, doi:10.1175/JPO2875.1.
- Talley, L. D., and M. S. McCartney, 1982: Distribution and circulation of Labrador Sea Water. *J. Phys. Oceanogr.*, **12**, 1189–1205, doi:10.1175/1520-0485(1982)012<1189:DACOLS>2.0.CO;2.
- Treguier, A. M., S. Theetten, E. P. Chassignet, T. Penduff, R. Smith, L. Talley, J. O. Beismann, and C. Böning, 2005: The North Atlantic subpolar gyre in four high-resolution models. *J. Phys. Oceanogr.*, **35**, 757–774, doi:10.1175/JPO2720.1.
- Våge, K., and Coauthors, 2009: Surprising return of deep convection to the subpolar North Atlantic Ocean in winter. *Nat. Geosci.*, **2**, 67–72, doi:10.1038/ngeo382.
- Visbeck, M., J. Marshall, and H. Jones, 1996: Dynamics of isolated convective regions in the ocean. *J. Phys. Oceanogr.*, **26**, 1721–1734, doi:10.1175/1520-0485(1996)026<1721:DOICRI>2.0.CO;2.
- , —, T. Haine, and M. Spall, 1997: Specification of eddy transfer coefficients in coarse-resolution ocean circulation models. *J. Phys. Oceanogr.*, **27**, 381–402, doi:10.1175/1520-0485(1997)027<0381:SOETCI>2.0.CO;2.
- Weaver, A. J., and T. M. C. Hughes, 1992: Stability and variability of the thermohaline circulation and its link to climate. *Trends in Physical Oceanography*, Research Trends Series, Vol. 1, Council of Scientific Research Integration, 15–70.
- White, M. A., and K. J. Heywood, 1995: Seasonal and interannual changes in the North Atlantic subpolar gyre from Geosat and TOPEX/POSEIDON altimetry. *J. Geophys. Res.*, **100**, 24 931–24 941, doi:10.1029/95JC02123.
- Yang, D., and O. A. Saenko, 2012: Ocean heat transport and its projected change in CanESM2. *J. Climate*, **25**, 8148–8163, doi:10.1175/JCLI-D-11-00715.1.
- Yashayaev, I., 2007: Hydrographic changes in the Labrador Sea, 1960–2005. *Prog. Oceanogr.*, **73**, 242–276, doi:10.1016/j.pocean.2007.04.015.
- , and J. W. Loder, 2009: Enhanced production of Labrador Sea Water in 2008. *Geophys. Res. Lett.*, **36**, L01606, doi:10.1029/2008GL036162.
- , H. M. van Aken, N. P. Holliday, and M. Bersch, 2007: Transformation of the Labrador Sea Water in the subpolar North Atlantic. *Geophys. Res. Lett.*, **34**, L22605, doi:10.1029/2007GL031812.
- Yu, L., R. A. Weller, and B. Sun, 2004: Improving latent and sensible heat flux estimates for the Atlantic Ocean (1988–99) by a synthesis approach. *J. Climate*, **17**, 373–393, doi:10.1175/1520-0442(2004)017<0373:ILASHF>2.0.CO;2.